ACS NANO

www.acsnano.org

ARTICLE

Tough MXene-Cellulose Nanofibril Ionotronic Dual-Network Hydrogel Films for Stable Zinc Anodes

Mengyu Liu, Liming Zhang,* Jowan Rostami, Teng Zhang, Kyle Matthews, Sheng Chen, Wenjie Fan, Yue Zhu, Jingwei Chen, Minghua Huang, Jingyi Wu, Huanlei Wang,* Mahiar Max Hamedi,* Feng Xu,* Weiqian Tian,* Lars Wågberg, and Yury Gogotsi

Cite This: *ACS Nano* 2025, 19, 13399−13413

Read Online

ACCESS | Metrics & More | Article Recommendations | Supporting Information

ABSTRACT: Developing ionotronic interface layers for zinc anodes with superior mechanical integrity is one of the efficient strategies to suppress the growth of zinc dendrites in favor of the cycling stability of aqueous zinc-ion batteries (AZIBs). Herein, we assembled robust 2D MXene-based hydrogel films cross-linked by 1D cellulose nanofibril (CNF) dual networks, acting as interface layers to stabilize Zn anodes. The MXene-CNF hydrogel films integrated multifunctionalities, including a high in-plane toughness of 18.39 MJ m^{-3}, high in-plane/out-of-plane elastic modulus of 0.85 and 3.65 GPa, mixed electronic/ionic (ionotronic) conductivity of 1.53 S cm^{-1} and 0.52 mS cm^{-1}, and high zincophilicity with a high binding energy (1.33 eV) and low migration energy barrier (0.24 eV) for Zn^{2+}. These integrated multifunctionalities, endowed with coupled multifield effects, including strong stress confinement and uniform ionic/electronic field distributions on Zn anodes, effectively suppressed dendrite growth, as proven by experiments and simulations. An example of the MXene-CNF|Zn showed a reduced nucleation overpotential of 19 mV, an extended cycling life of over 2700 h in Zn||Zn cells, and a high capacity of 323 mAh g^{-1} in Zn||MnO_2 cells, compared with bare Zn. This work offers an approach for exploring mechanically robust 1D/2D ionotronic hydrogel interface layers to stabilize the Zn anodes of AZIBs.

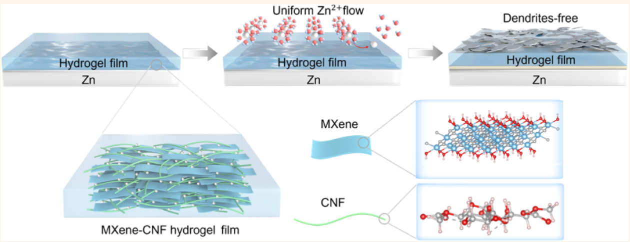

KEYWORDS: *Ionotronic hydrogel, MXene, cellulose nanofibrils, interface layers, zinc anodes*

Downloaded via KTH ROYAL INST OF TECHNOLOGY on March 5, 2026 at 14:57:17 (UTC).
See https://pubs.acs.org/sharingguidelines for options on how to legitimately share published articles.

Rechargeable aqueous zinc-ion batteries (AZIBs), among various energy storage systems, have drawn considerable attention due to their high safety, low price, low redox potential (−0.76 V versus standard hydrogen electrode), and high theoretical capacity (820 mAh g^{-1}) of Zn anodes.[1−7] However, the intrinsic coarse surfaces of Zn metal can cause uneven electric/ionic field distribution on the Zn anodes, generating heterogeneous Zn depositions, gradually evolving into Zn dendrites during prolonged charging/discharging.[8,9] The Zn dendrites may pierce the separators, eventually causing short circuits in the AZIBs. Synchronously, the long-term charging/discharging cycles inevitably form nonconductive byproducts, which further increase surface roughness and produce poor interfacial charge transport on the surfaces of Zn anodes. The above process further consumes the electrolyte and Zn^{2+} leading to low Coulombic efficiency (CE) and poor reversibility.[10] Additionally, the hydrogen evolution reaction (HER), competing with the zinc deposition reaction, can occupy active sites and reduce the current available for zinc deposition, thus decreasing the CE.[11] HER can also cause additional electrolyte consumption and gas expansion, which impairs the cycle life of AZIBs.[12] These undesirable consequences seriously hinder the practical application of AZIBs.

Recently, some strategies have been reported to solve the above challenges, including developing novel separators,[3] optimizing electrolytes,[13,14] and constructing artificial interfaces on Zn anodes.[8,15−18] Notably, constructing artificial interfaces on Zn anodes is one of the effective strategies to induce uniform Zn^{2+} deposition and suppress the formation of dendrites and byproducts. Various artificial interface layers have been reported to date, such as zinc alginate hydrogel,[16] layer-by-layer assembled chitosan/sodium alginate,[18] stearic

Received: January 23, 2025
Revised: March 18, 2025
Accepted: March 18, 2025
Published: March 25, 2025

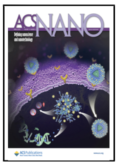

© 2025 American Chemical Society

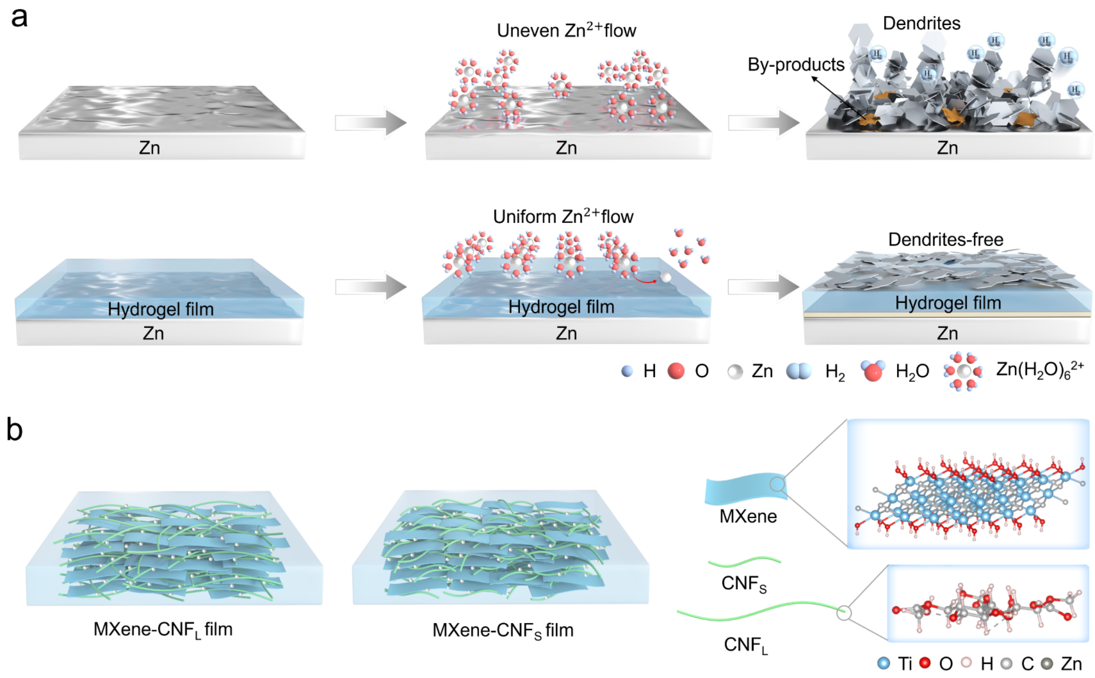

Figure 1. (a) Schematic illustration of the Zn^{2+} deposition behaviors on bare Zn and MXene-CNF|Zn anodes. (b) Schematic illustration of the microstructures of MXene-CNF hydrogel films.

acid-modified Cu nanorods,[8] and MXene-based composites.[15,17,19] More interestingly, the robust interface layers can contain the stress induced by volume changes, dendrite formation, and gas generation during charging and discharging.[15,19] However, all reported studies of artificial interface layers for Zn anodes have never explored their mechanical properties in aqueous electrolytes and have never evaluated their stress confinement effects for suppressing dendrite growth, to the best of our knowledge. Therefore, developing artificial ionotronic interface layers for Zn anodes with superior mechanical properties in aqueous electrolytes is a promising strategy to address the above challenges of AZIBs.

Renewable 1D nanocellulose, such as cellulose nanofibrils (CNF), can reinforce 2D nanosheets to assemble macroscopic 1D/2D nanocomposite films with high mechanical properties, where the stiff 2D nanosheets are entangled into the interconnected networks of 1D nanocellulose.[20−25] $Ti_3C_2T_x$ MXene as a well-known 2D nanomaterial, has been widely used in the assembly of multifunctional films due to its metallic conductivity, intrinsic mechanical properties, hydrophilicity, and abundant terminal groups (−O, −OH, or −F),[26−30] etc. Herein, we tailored the aspect ratios of CNF (with high aspect ratios denoted as CNF_L and low aspect ratios as CNF_S), the CNF contents, and their cross-linking networks to assemble MXene-based 1D/2D nanocomposite hydrogel films, where the flexible cross-linked CNF, acting as adhesives and matrixes, offered dual network interactions of numerous physical entanglements and Zn^{2+} cross-linking for stiff MXene nanosheets, improving the macroscopic mechanical properties. An example of as-assembled MXene-CNF_L hydrogel films with a CNF_L content of 40 wt % (denoted as MXene-40%CNF_L) in 2 M $ZnSO_4$ showed high in-plane mechanical properties, including a tensile strength of 37.55 MPa at an elongation of 23.83%, a toughness of 7.67 MJ m^{-3}, and Young's modulus of 0.85 GPa, a high out-of-plane Young's modulus of 3.65 GPa, and high ionotronic properties with a mixed electronic/ionic conductivity of 1.53 S cm^{-1} and 0.52 mS cm^{-1}, respectively. The integrated multifunctionalities, enabling the MXene-CNF_L hydrogel films as robust interface layers for Zn anodes (Figure 1), can offer strong stress confinement to suppress Zn dendrite growth, contain the volume changes during Zn plating/stripping, and homogenize Zn^{2+} flow and electrical field distribution on Zn anodes, which were supported by experimental results and corresponding finite element calculations of the stress−strain field, ionic field, and electronic field. Electrochemical characterizations revealed that MXene-40%CNF_L|Zn electrodes had a lower overpotential (19 mV) and a more negative hydrogen evolution potential (−0.21 V) than that of bare Zn. The MXene-40%CNF_L|Zn||MXene-40% CNF_L|Zn symmetrical cells delivered a long cycle life of over 2700 h and flat deposition behavior of Zn^{2+} on Zn anodes. These results were further supported by density functional theory (DFT) calculations, which exhibited higher zincophilicity with a larger binding energy (−1.33 eV) and a lower migration energy barrier (0.24 eV) for Zn atoms on MXene-CNF_L|Zn anodes than bare Zn anodes. Practical full cells of MXene-40%CNF_L|Zn||MnO_2 showed a low charge transfer resistance of 2.50 Ω, a high discharge specific capacity of 323 mAh g^{-1} and 119 mAh g^{-1} at 0.2 A g^{-1} and 3 A g^{-1}, respectively, and a high retention of 92.8% capacity after resting for 24 h.

RESULT AND DISCUSSION

We fabricated two types of wood-derived CNF with similar widths of 1.77 nm for CNF_L and 1.93 nm for CNF_S, but with different lengths: CNF_L with a high aspect ratio (l/w) of 524 and CNF_S with a lower aspect ratio of 210 (Figures 1b, 2a,b, and S1a,b), to assemble $Ti_3C_2T_x$ MXene nanosheets. The prepared $Ti_3C_2T_x$ MXene monolayers showed an average thickness of 1.91 nm (Figures 2c and S1c) and an average lateral size of around 600 nm. The aqueous dispersions of CNF and MXene, as well as their mixed dispersions, presented high

https://doi.org/10.1021/acsnano.5c01497

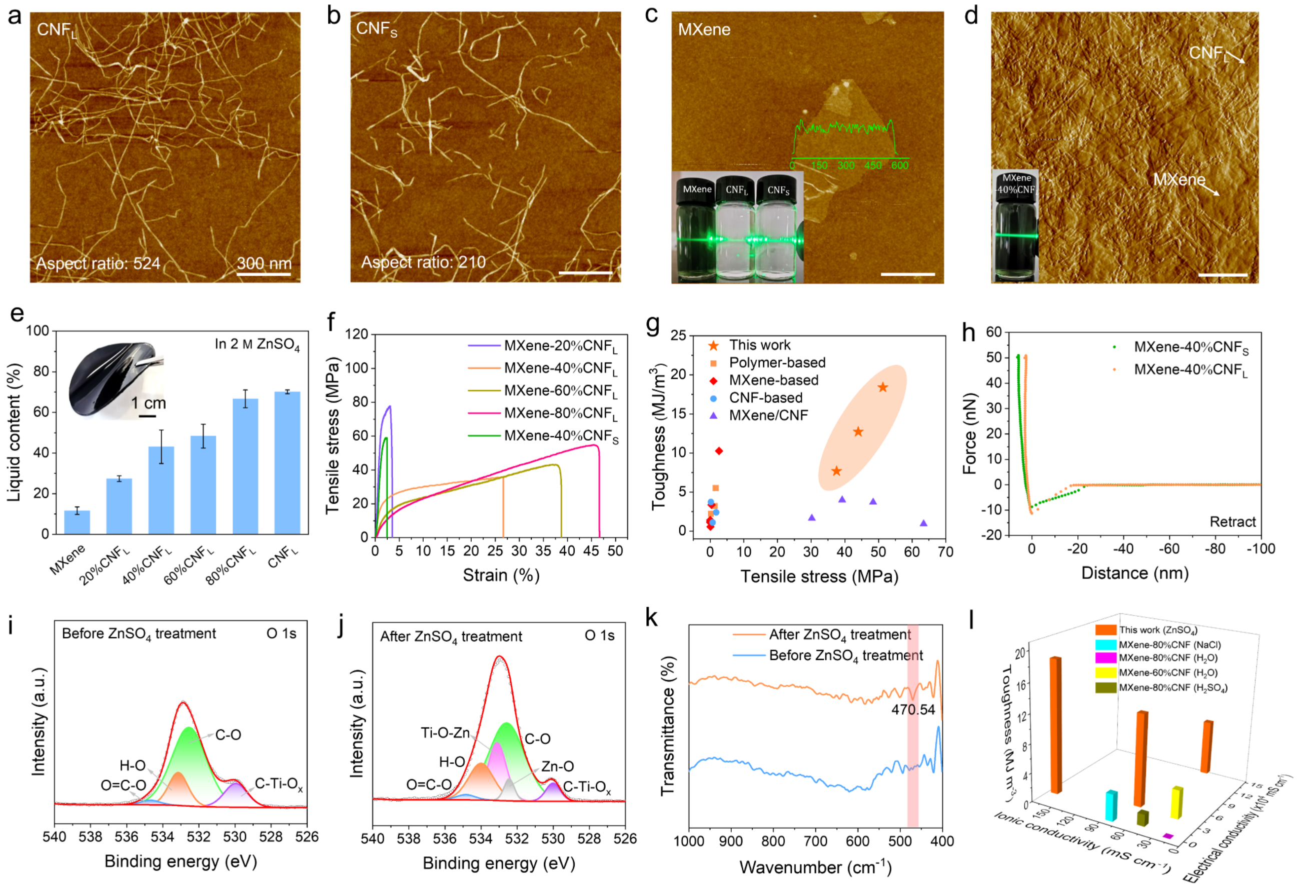

Figure 2. Fabrication and characterization of mechanically robust MXene-CNF ionotronic hydrogel films. AFM height images of (a) CNF$_L$, (b) CNF$_S$, and (c) MXene, and (d) AFM peak-force error image of MXene-40%CNF$_L$ films, with a scale bar of 300 nm. (Inset c) Digital photos of the Tyndall effect of CNF$_L$, CNF$_S$, and MXene colloidal dispersions, and (inset d) of mixed MXene-40%CNF$_L$ colloidal dispersion. (e) Liquid content of MXene-CNF$_L$ hydrogel films with different compositions after 2 M ZnSO$_4$ treatment for 24 h and (inset e) digital photo of MXene-CNF$_L$ hydrogel film. (f) Representative tensile stress−strain curves of different MXene-CNF$_L$ hydrogel films. (g) Comparison of the toughness and tensile stress of MXene-CNF$_L$ hydrogel films with reported hydrogels.[20,32−34,46−52] (h) AFM indentation profiles of MXene-40%CNF$_L$ and MXene-40%CNF$_S$ hydrogel films. XPS O 1s spectra of the MXene-40%CNF$_L$ (i) before and (j) after 2 M ZnSO$_4$ treatment. (k) Magnified FT-IR patterns of MXene-40%CNF$_L$ films before and after ZnSO$_4$ treatment. (l) Comparison of the toughness, and mixed ionic/electronic conductivity of MXene−CNF$_L$ hydrogel films with previously reported MXene−CNF hydrogel films.[20]

colloidal stability with obvious Tyndall effects (Figure 2c,d). We then used the mixed colloidal dispersions of MXene and CNF (see Experimental section) to assemble a series of MXene-CNF composite films by vacuum-assisted filtration. The obtained dry MXene-CNF films showed excellent mechanical integrity and distinct metallic luster and presented lamellar microstructures with a thickness of about 8 μm (Figure S2a,b). Atomic force microscopy (AFM) measurements (Figure 2d) showed that the high-aspect-ratio 1D nanofibrils offered densely interconnected networks to entangle 2D nanosheets, enabling mechanical properties higher than those of pure MXene films. For example, the dry MXene-40%CNF$_L$ films exhibited a high tensile strength of 292 MPa at a break elongation of 4.79%, higher than the films assembled from pure building blocks of MXene (64 MPa) and CNF$_L$ (250 MPa), and other MXene-CNF$_L$ films (Figure S3). Additionally, the MXene-CNF films displayed smooth surfaces (Figures S4 and S5), such as a low R_a roughness of 10.9 nm for MXene-40%CNF$_L$, beneficial to the uniform deposition of Zn^{2+} to inhibit the tip effect[3,18] when the MXene-CNF films acted as interface layers for Zn anodes.

The MXene-CNF$_L$ films were immersed in an aqueous solution of 2 M $ZnSO_4$, and the films were then transformed into hydrogels by absorbing a plenty of solution that can reach a liquid content of up to 60 wt % (Figure 2e). This was attributed to the reinforced CNF networks in MXene-CNF$_L$ films with strong capacities for adsorbing and retaining water.[31] All MXene-CNF$_L$ hydrogel films maintained macroscopic mechanical integrity, even after bath ultrasonication. In contrast, the pure MXene films began to disrupt immediately after immersion in the solution until redispersal completely (Figure S6). This was attributed to the toughening effect of the cross-linked CNF networks.

We first evaluated the toughening effect of different CNF$_L$ contents for MXene-CNF hydrogel films (Figure 2f and Table S1). The results revealed that the toughness of hydrogel films increased with CNF$_L$ content, where the MXene-80%CNF$_L$ hydrogel films indeed showed the highest toughness of 18.39 MJ m^{-3} at an average tensile strength of 51.30 MPa and an average break elongation of 53.07% (Table S1), higher than some reported polymer-based hydrogels, such as poly(acrylic acid)/poly(3,4-ethylene-dioxythiophene):poly(styrene-sulfonate)/MXene (3.36 MJ m^{-3} at a tensile strength of 0.38

https://doi.org/10.1021/acsnano.5c01497
ACS Nano 2025, 19, 13399−13413

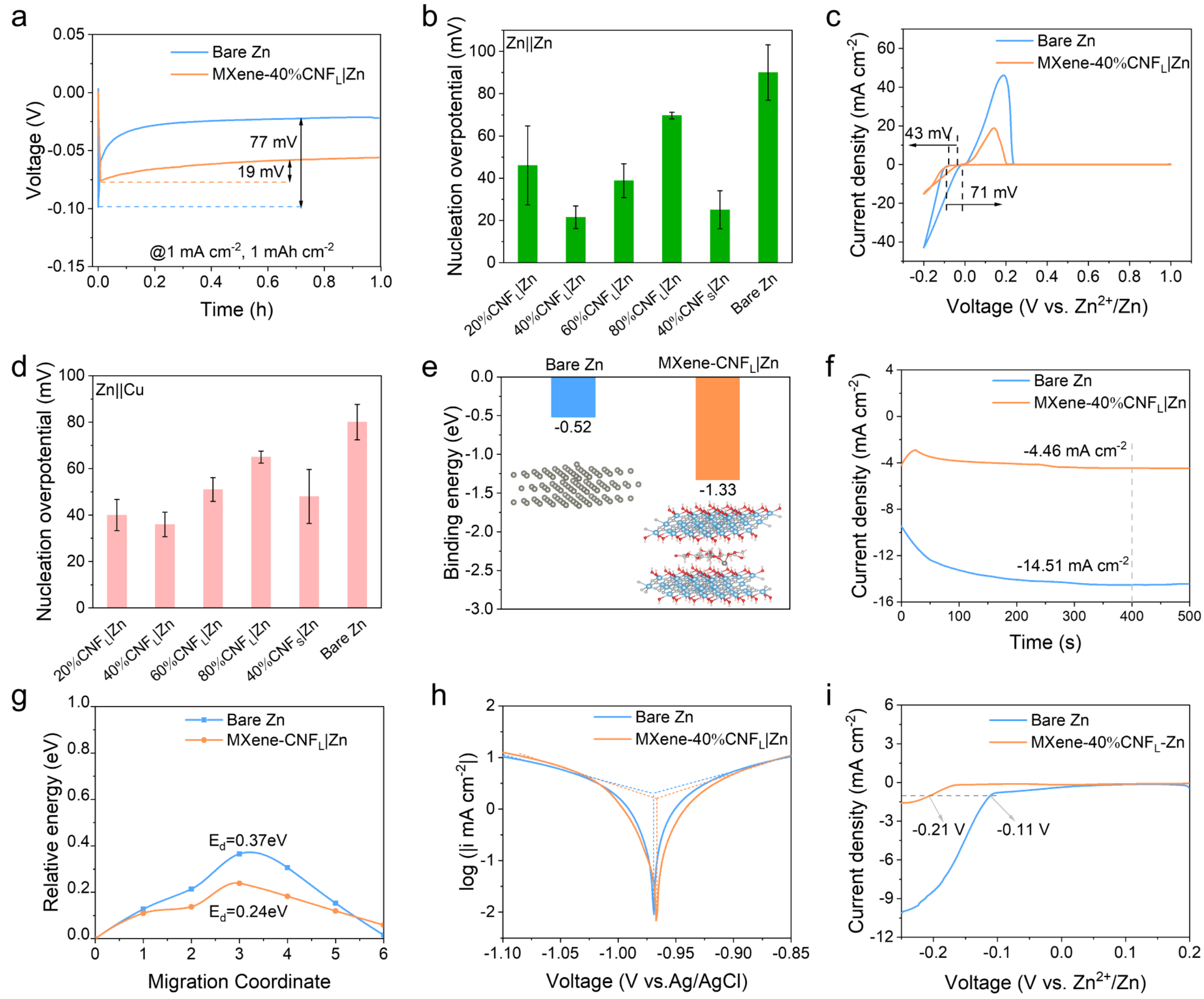

Figure 3. Electrochemical effects of mechanically robust MXene-CNF ionotronic hydrogel films as interface layers on Zn anodes. (a) Nucleation overpotential profiles of Zn plating on bare Zn and MXene-40%CNF$_L$|Zn electrodes, and (b) corresponding nucleation overpotential values of bare Zn, MXene-CNF$_L$|Zn with different CNF$_L$ contents, and MXene-40%CNF$_S$|Zn electrodes. (c) CV curves of Zn||Cu cells with bare Zn and MXene-40%CNF$_L$|Zn anodes at a scan rate of 1 mV s^{-1}, and (d) corresponding nucleation overpotentials of bare Zn, MXene-CNF$_L$|Zn with different CNF$_L$ contents, and MXene-40%CNF$_S$|Zn anodes. All the error bars in b and d are the standard deviations calculated from more than three repeated measurements. (e) The binding energies of Zn atoms on bare Zn and MXene-CNF$_L$|Zn from DFT calculations. (f) Chronoamperograms of bare Zn and MXene-40%CNF$_L$|Zn electrodes in Zn||Zn symmetrical cells. (g) Migration energy barrier (E_d) of Zn^{2+} on the bare Zn and MXene-CNF$_L$|Zn anodes calculated by DFT. (h) Tafel curves of the bare Zn, and MXene-40% CNF$_L$|Zn anodes at a scan rate of 1 mV s^{-1}. (i) Hydrogen evolution potentials measured by Zn||SS cells in 1 M Na$_2$SO$_4$ with a scan rate of 1 mV s^{-1}.

MPa),[32] poly(vinyl alcohol)/chitosan/CNF/muriate of potash (2.39 MJ m^{-3} at 1.78 MPa),[33] and polyacrylamide/alginate/polypyrrole hydrogels (5.5 MJ m^{-3} at 1.63 MPa) (Figure 2g and Table S2).[34] The toughening effect of CNF was further supported by the fracture morphologies of MXene-CNF$_L$ films (Figure S7), where the fracture edges changed from stepped lamellar microstructures to crimped and zigzag structures with increasing CNF$_L$ content, due to the stronger reinforced network interaction between CNF and MXene nanosheets.[27] More interestingly, the X-ray photoelectron spectroscopy (XPS) analysis showed the successful incorporation of Zn^{2+} into the MXene-CNF$_L$ films after treatment in 2 M ZnSO$_4$, by appearing characteristic peaks of the Zn 2p$_3$/$_2$ at 1022 eV and Zn 2p$_1$/$_2$ at 1046 eV (Figure S8).[35] Notably, the O 1s XPS spectrum of MXene-CNF$_L$ films after ZnSO$_4$ treatment depicted enhanced peak intensity and appeared new peaks at 533.11 eV corresponding to Ti−O−Zn bonds and 532.44 eV for Zn−O bonds (Figure 2i,j, and Table S3).[36−39] Fourier transform infrared (FT-IR) spectra also featured a pronounced peak that emerged at 470.54 cm^{-1} for the MXene-CNF$_L$ films after ZnSO$_4$ treatment (Figure 2k and Figure S9), which is attributed to the Zn−O stretching vibration.[36,40,41] The analysis from XPS and FT-IR spectra both indicated the formation of Zn−O bonds between incorporated Zn^{2+} and the matrix components of the MXene nanosheets and CNF$_L$, which may act as chemically cross-linked bridges between CNF and MXene nanosheets (Figure S10). The cross-linked bridging interactions contributed to the formation of more robust and stable hydrogel networks to improve the mechanical and structural integrity of the MXene-CNF$_L$ hydrogel films and their resistance to degradation in an electrochemical environment. This was in line with the wet mechanical properties of pure CNF films cross-linked by multivalent metal ions, such as Fe^{3+} or Al^{3+} , as counterions to balance the charges of the anionic CNFs.[42]

The toughening effect of the aspect ratios of CNF was also investigated, where low-aspect-ratio CNF_S was used to assemble the control samples of MXene-CNF_S hydrogel films. Interestingly, with the same CNF content, the MXene-40%CNF_L hydrogel films showed a toughness of 7.67 MJ m^{-3} at an elongation at break of 23.83%, more than 5-fold higher than that of the control sample of MXene-CNF_S with a toughness of 1.45 MJ m^{-3} at 2.68% (Figure 2f and Table S1). The results indicated that CNF_L presented a stronger toughening effect for MXene-CNF hydrogel films than CNF_S because of the higher aspect ratio of CNF_L, which is in favor of forming more physically entangled networks.[43,44] Additionally, MXene-40%CNF_L hydrogel films showed an in-plane Young's modulus of 0.85 GPa in the elastic deformation region and an out-of-plane Young's modulus of 3.65 GPa, measured by AFM indentation perpendicular to the surfaces of the hydrogel films (Figures 2h, S11, and S12). The high toughness and in-plane/out-of-plane stiffness suggested that the MXene-CNF_L hydrogel films, as interface layers, can offer strong stress confinement effects on the surfaces of Zn anodes, which generated mechanical suppression for the volume changes and dendrite growth during charging and discharging.[15,19] The MXene-CNF_L films also showed smaller contact angles than bare Zn foils (Figure S13), indicating that the MXene-CNF_L films, as interface layers, can better equalize the Zn^{2+} flux of the aqueous electrolyte across the interfacial layers to realize uniform Zn^{2+} deposition on Zn anodes.[16,45]

The ionotronic properties of MXene-CNF_L hydrogel films were then evaluated using the four-point probe method for electronic conductivity and electrochemical impedance spectroscopy (EIS) for ionic conductivity (Figure S14 and Table S1). The results indicated that the CNF content in the MXene-CNF_L hydrogel films can modulate their ionotronic properties, where an enhanced CNF_L content resulted in increased ionic conductivity but decreased electronic conductivity. For example, MXene-80%CNF_L hydrogel films presented the highest ionic conductivity of 1.67 mS cm^{-1} but the lowest electronic conductivity of 210.71 mS cm^{-1}. In contrast, the MXene-20%CNF_L hydrogel films showed the highest electronic conductivity of 1.86×10^4 mS cm^{-1} but with negligible ionic conductivity. Notably, MXene-40%CNF_L hydrogel films showed highly integrated ionotronic properties with an electronic conductivity of 1.53 S cm^{-1} and an ionic conductivity of 0.52 mS cm^{-1}, enabling the MXene-CNF_L hydrogel films to serve as potential mixed ionic-electronic conductors, comparable to the most advanced mixed ionic-electronic conductors reported to date (Table S4).[20] We systematically compared the toughness and the mixed ionic/electronic conductivity of MXene-CNF_L hydrogel films with previous reports (Figure 2l), indicating that the family of MXene-CNF_L hydrogel films presented an excellent integration of high mechanical toughness and high ionotronic properties. The above results indicated that the as-fabricated MXene-CNF_L hydrogel films can act as promising interface layers for stabilizing Zn anodes in AZIBs.

We investigated the electrochemical effect of mechanically robust MXene-CNF_L ionotronic hydrogel films as interface layers on Zn anodes. The nucleation overpotentials of Zn plating on different MXene-CNF_L|Zn electrodes were obtained from the galvanostatic charging/discharging profiles of symmetric Zn||Zn cells at a current density of 1 mA cm^{-2} for an areal capacity of 1 mAh cm^{-2} (Figures 3a and S15). All MXene-CNF_L|Zn electrodes depicted much lower nucleation overpotentials, more interestingly, with the MXene-40%CNF_L|Zn showing the lowest value of 19 mV, compared with the control samples of bare Zn (77 mV) and MXene-40%CNF_S|Zn (34 mV) (Figure 3b). Additionally, the MXene-40%CNF_L|Zn still exhibited a lower nucleation overpotential of 64 mV, compared with that of bare Zn at 129 mV, even at a high current density of 5 mA cm^{-2} for 2.5 mAh cm^{-2} (Figure S16). The results were consistent with the cyclic voltammetry (CV) measurements of the Zn||Cu half cells (Figures 3c,d, and S17), where the MXene-40%CNF_L|Zn anodes also presented the lowest nucleation overpotential of 43 mV compared to other MXene-CNF|Zn and bare Zn anodes. Furthermore, the MXene-40%CNF_L hydrogel films exhibited excellent integrated multifunctionalities, including a high out-of-plane/in-plane Young's modulus of 3.65 GPa/0.85 GPa, high in-plane toughness of 7.67 MJ m^{-3} at a break elongation of 23.83%, and mixed electronic/ionic conductivity of 1.53 S cm^{-1}/0.52 mS cm^{-1} (Table S1). We thus chose MXene-40%CNF_L as a representative of all MXene-CNF_L hydrogel films to further investigate their potential for stabilizing Zn anodes in this work. The DFT calculation corroborated the above experimental results (Figure 3e), simulating the binding energy between the Zn atom and the anodes, and showing the MXene-CNF_L|Zn anodes with a higher binding energy of −1.33 eV than the bare Zn anode at −0.52 eV. This resulted from the abundant surface functional groups (−OH, −COOH, etc.) of MXene-CNF_L hydrogel interface layers, which afforded abundant zincophilic sites and thus generated higher zincophilicity than bare Zn anodes. The decreased nucleation overpotential and higher zincophilicity of the MXene-CNF_L|Zn anodes indicated a lower nucleation barrier and faster nucleation dynamics than bare Zn, which can boost Zn^{2+} deposition and reduce polarization on Zn anodes.[16] The above results also suggested that modulating the contents and aspect ratios of CNF in the MXene-CNF hydrogel interface layers can tune the initial deposition behaviors of Zn^{2+} and thus electrochemical performance of the Zn anodes.

To further investigate the deposition behaviors of Zn^{2+} on different Zn anodes, chronoamperometry (CA) tests of symmetrical Zn||Zn cells were conducted at an overpotential of −150 mV (Figure 3f) to monitor the response current over time, which was highly dependent on the surface-states of the Zn electrodes.[8,9,54] The MXene-40%CNF_L|Zn electrodes showed a short variation region of the response current and a stable current density of 4.46 mA cm^{-2} within 400 s, much lower than the bare Zn electrodes, which gradually stabilized at 14.51 mA cm^{-2} within 400 s. The shorter initial current variation stood for the less 2D diffusion state, where the footprint of Zn^{2+} deposition was confined to the vicinity of the initial nucleation sites that caused Zn^{2+} accumulation and further boosted the formation of Zn dendrites.[9,14] The lower stable section of the response current represented a 3D diffusion state, where Zn^{2+} was uniformly deposited on the surface of the Zn electrodes, inhibiting the tip effect and the generation of Zn dendrites.[55−57] The above results thus illustrated that the MXene-40%CNF_L|Zn electrodes shortened the 2D diffusion time and had dominantly 3D diffusion states, with less charge accumulation and uniform Zn^{2+} deposition, boosting the Zn^{2+} migration and suppressing the growth of Zn dendrites. This outcome was further supported by DFT

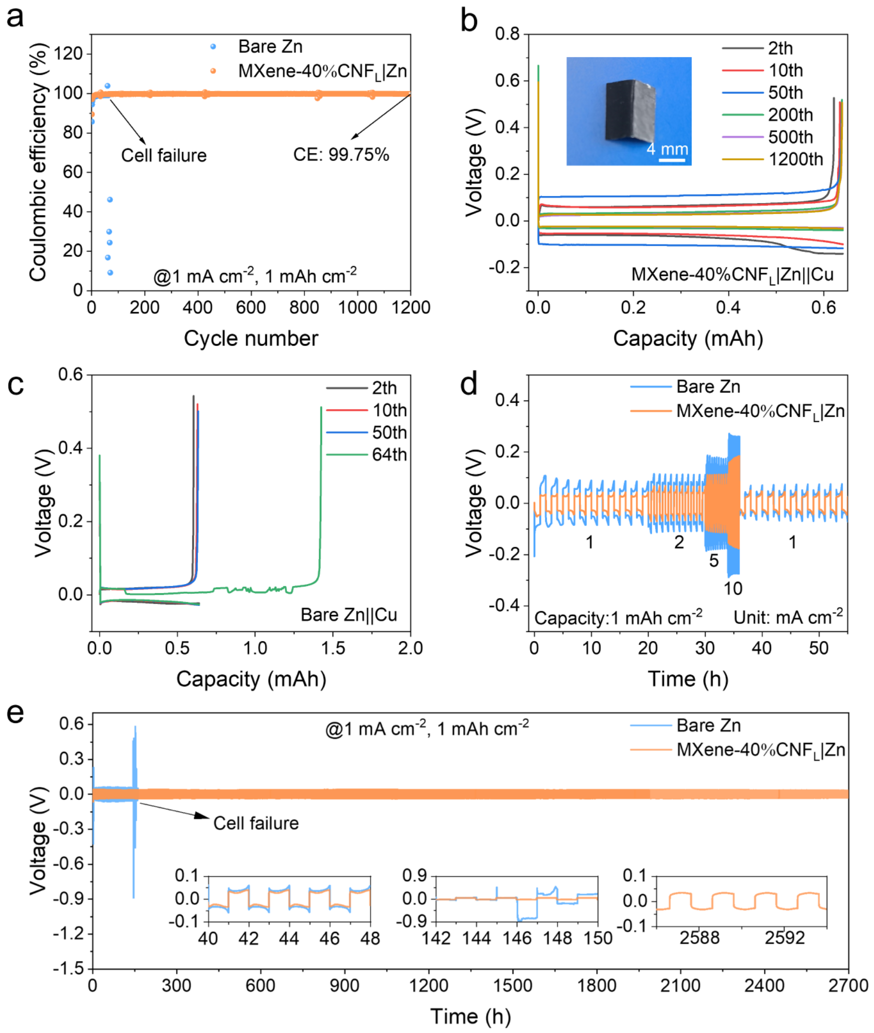

Figure 4. Electrochemical performance of the Zn||Zn and Zn||Cu cells. (a) Coulombic efficiencies of Zn||Cu half cells at a current density of 1 mA cm^{-2} for an areal capacity of 1 mAh cm^{-2}. Charging/discharging profiles of (b) MXene-40%CNF$_L$-Zn||Cu and (c) bare Zn||Cu half cells at different cycles at 1 mA cm^{-2} for 1 mAh cm^{-2}. (Inset b) Optical photograph of the MXene-40%CNF$_L$ film after 100 charging/discharging cycles. (d) Rate performance of Zn||Zn symmetrical cells at current densities of 1, 2, 5, and 10 mA cm^{-2} for 1 mAh cm^{-2}. (e) Cycling performance of the Zn||Zn symmetrical cells at 1 mA cm^{-2} for 1 mAh cm^{-2}, and (inset e) magnified charging/discharging profiles at different cycles.

calculations, where the Zn^{2+} migration path was simulated using the NEB method (Figures 3g and S18). The MXene-CNF$_L$|Zn electrodes showed a migration energy barrier of 0.24 eV for Zn^{2+} that was lower than that of the bare Zn electrodes (0.37 eV). The facilitated migration of Zn^{2+} in the MXene-CNF$_L$|Zn electrodes was attributed to the abundant hydroxyl and carboxylate groups, along with high-aspect-ratio 1D CNF$_L$ intercalated among 2D MXene nanosheets, providing more hopping sites for Zn^{2+} migration by additional coordination sites and ion−ion/ion−dipole interactions,[58] and also resulted from the hierarchical 1D/2D heterostructures offering more diffusion channels for Zn^{2+} transport.

We explored the capability of MXene-CNF hydrogel films as interface layers to protect the Zn anodes from surface corrosion and HER, which can generate uneven topological morphologies and further promote dendrite formation to shorten the life of AZIBs.[18,59] We used the Tafel curves obtained from the potentiodynamic polarization technique to characterize the corrosion resistance of the MXene-CNF$_L$ interface layers in a 2 M $ZnSO_4$ electrolyte (Figure 3h). The MXene-40%CNF$_L$|Zn electrode showed a positive shift in corrosion potential (−0.967 V) compared with bare Zn anodes (−0.969 V) and a lower corrosion current density of 1.58 mA cm^{-2} than the bare Zn (2.01 mA cm^{-2}), indicating that the MXene-40%CNF$_L$ interface layers inhibited the corrosion reaction and decreased the corrosion rate on the surfaces of Zn anodes.[60,61] This may be attributed to the numerous hydrophilic terminal groups in the MXene-CNF$_L$ hydrogel films bonding with the coordinating water molecules of $Zn(H_2O)_6^{2+}$,[16,62,63] thereby reducing the direct contact of water molecules with the surfaces of Zn anodes and decreasing corrosion.[64] We used linear sweep voltammetry (LSV) measurements to evaluate the performance of HER and the oxygen evolution reaction (OER) (Figures 3i, S19, and S20). The MXene-40%CNF$_L$|Zn anodes presented a more negative HER potential of −0.21 V (vs Zn^{2+}/Zn) than the bare Zn anode (−0.11 V vs Zn^{2+}/Zn) at a current density of −0.5 mA cm^{-2} and had a wider electrochemical window, indicating that the MXene-40%CNF$_L$ interface layers effectively inhibited water electrolysis on Zn anodes and thereby improved the lifespan of the AZIBs.[65]

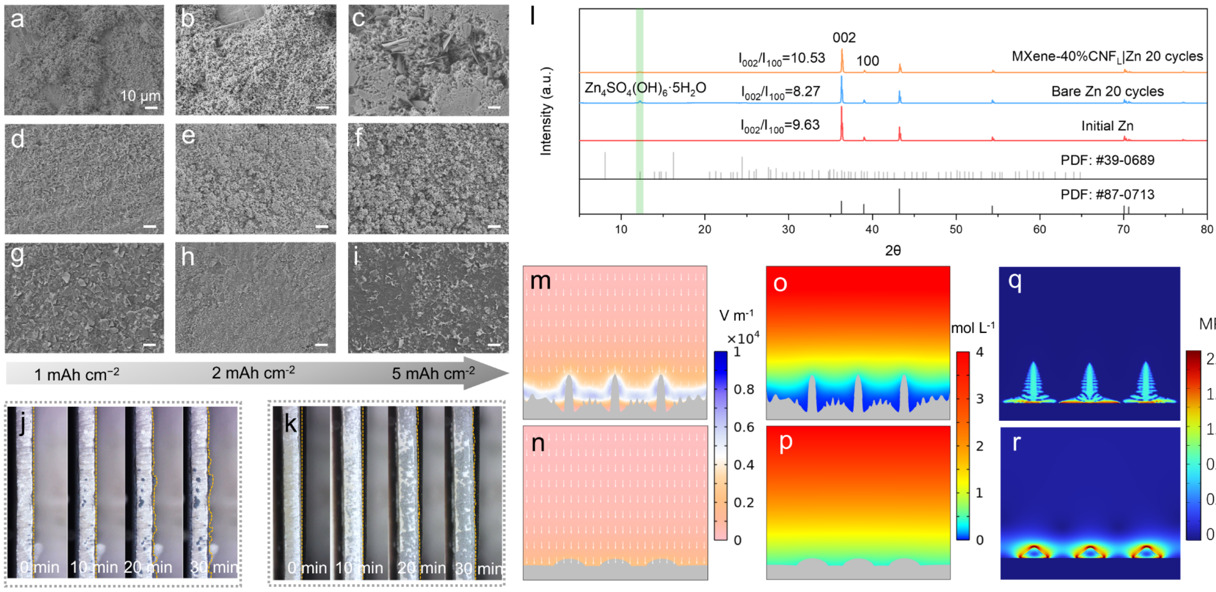

Figure 5. **Characterization and simulation of the multifield effects of MXene-CNF$_L$hydrogel interface layers on Zn deposition. SEM images (all scale bars of 10 μm) of the deposition morphology on (a−c) bare Zn anodes, and on (d−f) the Zn surfaces and (g−i) MXene-40%CNF$_L$ film surfaces of MXene-40%CNF$_L$|Zn anodes, at 1 mA cm^{-2} for 1, 2, and 5 mAh cm^{-2}. *In situ* optical microscopy photos of (j) bare Zn and (k) MXene-40%CNF$_L$|Zn at 10 mA cm^{-2} for 30 min. (l) X-ray diffraction (XRD) patterns of different Zn electrodes after the first 20 cycles. Finite element calculation of (m,n) electric field, (o,p) Zn^{2+} concentration field, and (q,r) stress field distributions on (m,o,q) bare Zn and (n,p,r) MXene-CNF$_L$|Zn electrodes.**

The plating/stripping behaviors of Zn^{2+}/Zn were then investigated by using charging/discharging tests of the Zn||Cu half cells. The MXene-40%CNF$_L$|Zn||Cu half cells had a high CE of 99.75% after 1200 cycles (Figure 4a), and their voltage-capacity profiles remained flat without evident fluctuation even at the 1200th cycle (Figure 4b). In contrast, the bare Zn||Cu half cells displayed a poor cycle life of around 60 cycles, with the voltage-capacity profiles already exhibiting huge fluctuations even at the 64th cycle (Figure 4c). The reversibility and cycle stability of MXene-40%CNF$_L$|Zn electrodes were further investigated by using charge/discharge measurements in Zn||Zn symmetrical cells. The MXene-40%CNF$_L$|Zn||MXene-40%CNF$_L$|Zn cells showed higher rate capability and lower voltage hysteresis, ranging from 37 to 158 mV at current densities in the range from 1 to 10 mA cm^{-2} for a fixed areal capacity of 1 mAh cm^{-2}, compared with bare Zn||Zn symmetrical cells and MXene-40%CNF$_S$|Zn||MXene-40%CNF$_S$|Zn (Figures 4d and S21). Meanwhile, the MXene-40%CNF$_L$|Zn||MXene-40%CNF$_L$|Zn symmetrical cells presented significantly enhanced cycling stability under different charging/discharging conditions (Figures 4e and S22), such as at 1 mA cm^{-2} for 1 mAh cm^{-2} with a charging/discharging life of over 2700 h and a lower voltage hysteresis of about 37 mV, compared to bare Zn||Zn symmetrical cells, which had a short cycle life of about 145 h and a large voltage hysteresis of about 60 mV. The remarkable increase in cyclic stability and reversibility of MXene-40%CNF$_L$|Zn||MXene-40%CNF$_L$|Zn cells was attributed to the integrated multifunctional effects of MXene-CNF$_L$ hydrogel interface layers, which offered strong stress confinement for Zn^{2+} deposition, abundant zincophilic sites, and low Zn^{2+} migration energy barriers. Both of them induced more uniform Zn^{2+} deposition, a lower polarization voltage, and faster kinetics than bare Zn, to suppress the formation of "dead Zn" and Zn dendrites.

The multieffects of MXene-CNF$_L$ interface layers on the morphology evolution of Zn anodes were evaluated after cycling at 1 mA cm^{-2} for different areal capacities. The bare Zn anodes displayed uneven Zn deposition and evolved prominent Zn dendrites gradually with increased deposition capacity (Figure 5a−c), which supported the results of bare Zn symmetrical cells (Figure 4e) where the dendrites may pierce the separators. Notably, the MXene-40%CNF$_L$|Zn anodes exhibited uniform Zn deposition behaviors without flake-like byproducts on the surfaces of Zn anodes (Figure 5d−f) and the interface layers (Figures 5g−i and S23), even at a high areal capacity of 5 mAh cm^{-2}. We further employed *in situ* optical microscopy to directly observe the Zn deposition morphology on the Zn anodes during the charging processes at 10 mA cm^{-2}. The bare Zn appeared with distinct dendrites and bulges at the interfaces between the electrode and electrolyte as the charging process continued after 10 min (Figure 5j). In contrast, the interfaces of MXene-40%CNF$_L$|Zn maintained uniform zinc deposition even after 30 min (Figure 5k), indicating that the MXene-CNF$_L$ interface layers effectively suppressed dendritic growth to enhance the stability of Zn anodes. Additionally, the XRD pattern of bare Zn anodes after 20 cycles showed a byproduct peak at 12.23° (Figure 5l),[16,18] attributed to the formation of low-soluble $Zn_4(OH)_6SO_4 \cdot 5H_2O$ by the reaction between the Zn^{2+} ions released from the dissolution of Zn anodes and the SO_4^{2-}/OH^- from the electrolyte,[66] whereas the MXene-40%CNF$_L$|Zn anodes after 20 cycles were without the peak of byproducts, demonstrating that the MXene-40%CNF$_L$ interface layers inhibited the side reactions that form byproducts. More interestingly, the I_{002}/I_{100} ratio of bare Zn anodes decreased from 9.63 for initial Zn to 8.27 after 20 cycles and 7.6 after 50 cycles (Figure S24), suggesting that Zn deposition tended toward the (100) crystal plane, which is more prone to dendrite formation.[67] While the I_{002}/I_{100} ratio of MXene-40%CNF$_L$|Zn anodes increased to 10.53 after 20 cycles, indicating that the MXene-40%CNF$_L$ interface layers effectively induced Zn deposition along the (002) crystal plane to facilitate the planar nucleation, which

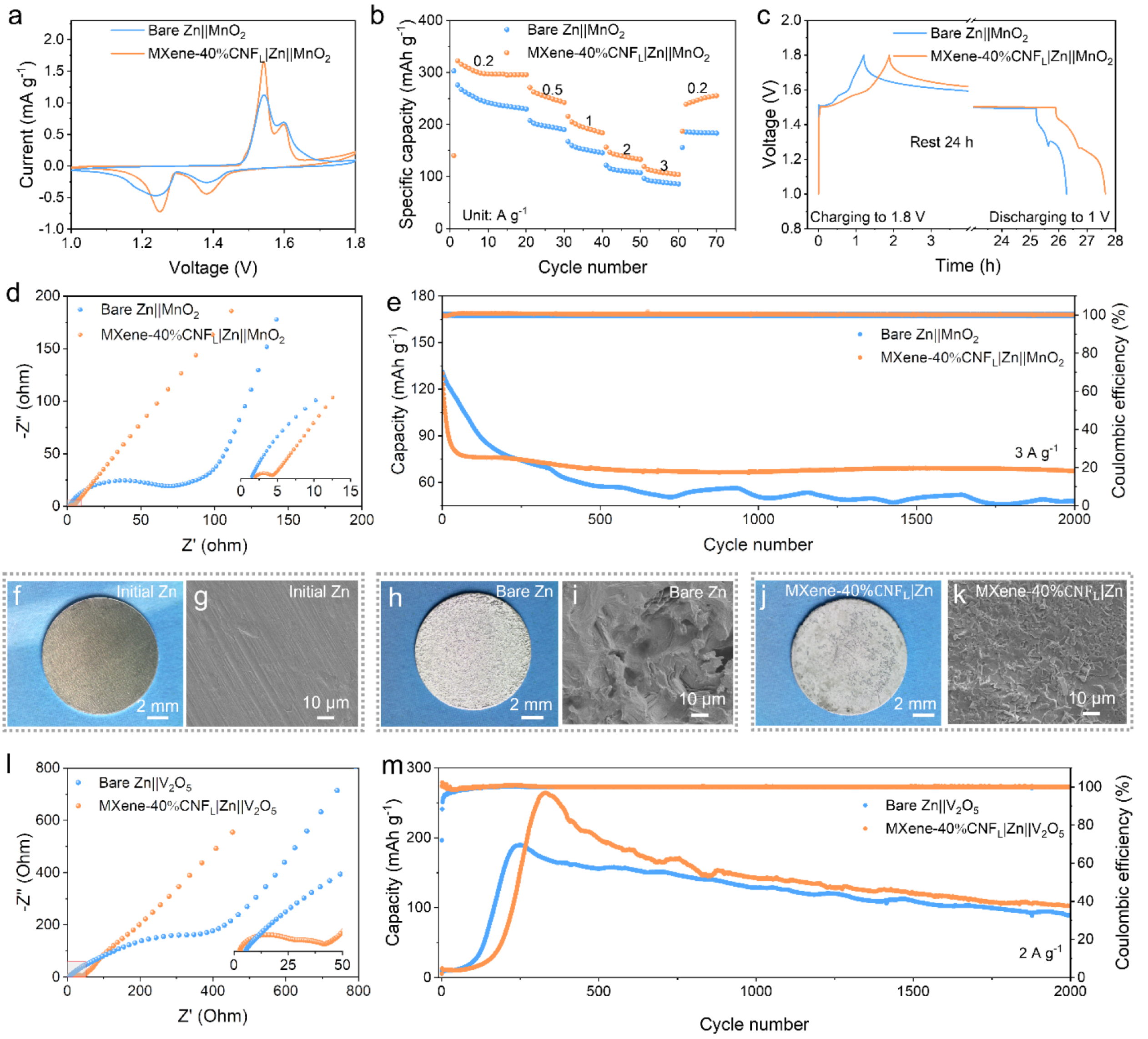

Figure 6. Electrochemical performance of the full cells for MXene-40%CNF$_L$|Zn||MnO$_2$ and MXene-40%CNF$_L$|Zn||V$_2$O$_5$. (a) CV curves of bare Zn||MnO$_2$ and MXene-40%CNF$_L$|Zn||MnO$_2$ full cells at a scan rate of 0.1 mV s^{-1}. (b) Rate performance at different current densities from 0.2 to 3 A g^{-1}, (c) self-discharging test after resting for 24 h, (d) Nyquist plots, and (e) long-term cycling performance at a high current density of 3 A g^{-1} for bare Zn||MnO$_2$ and MXene-40%CNF$_L$|Zn||MnO$_2$ full cells. Digital photographs (f,g,j) and corresponding SEM images (g,i,k) of (f,g) initial Zn foils, and the Zn surfaces of (h,i) bare Zn anodes and (j,k) MXene-40%CNF$_L$|Zn anodes in Zn||MnO$_2$ full cells after 2000 cycles. (l) Nyquist plots and (m) long-term cycling performance at 2 A g^{-1} of bare Zn||V$_2$O$_5$ and MXene-40%CNF$_L$|Zn||V$_2$O$_5$ full cells.

promoted uniform zinc deposition, and thus inhibited the dendrite growth.[14,37] The XRD outcomes were consistent with the CA measurements (Figure 3f) and the observations from the images of SEM and *in situ* optical microscopy (Figure 5a–k).

To further understand the Zn nucleation and deposition behaviors on the surface of different Zn anodes, we conducted theoretical simulations using finite element calculations to reveal the effects of MXene-CNF$_L$ hydrogel interface layers on the distribution of the electric field, Zn^{2+} concentration field, and stress–strain field (see the Experimental section, Figures S25–S28). The bare Zn anodes showed heightened intensity around the localized dendrite tips in the electric field (Figures 5m and S25a), commonly referred to as the "tip effect" which accelerated dendrite growth,[16] resulting from the inherent inhomogeneity of the bare Zn surfaces that brought about an uneven electric field distribution across the surface during Zn^{2+} deposition. Interestingly, with the incorporation of MXene-CNF$_L$ hydrogel interface layers, the surface of Zn anodes exhibited a uniform distribution of electric field intensity (Figures 5n and S25b), significantly in favor of diminishing the aggregation of zinc ions and reducing the possibility of dendrite formation.[13,16] The as-calculated Zn^{2+} concentration fields depicted the surfaces of bare Zn anodes with an evident concentration gradient (Figures 5o and S26a). In contrast, the MXene-CNF$_L$|Zn anodes presented a more uniform Zn^{2+} concentration field near the electrode surfaces (Figures 5p and S26b) and, especially, maintained a higher Zn^{2+} concentration (0.50–1 mol L^{-1}) than the bare Zn electrode (0–0.25 mol L^{-1}), where the enhanced Zn^{2+} flux provided a more constant supply of Zn^{2+} during their deposition, thus facilitating more homogeneous zinc deposition.[16] These results were attributed to the abundant zincophilic sites and lower Zn^{2+} migration barrier of the MXene-CNF$_L$ hydrogel interface layers, as calculated from DFT (Figure 3e−g), and were also ascribed to the superior mixed ionic/electronic conductivity (Table S1 and Figure 2l) where the favorable electronic conductivity contributed to enhancing Zn^{2+} reaction kinetics during deposition/stripping processes by accelerating charge transfer at the electrode−electrolyte interface,[53] and the improved ionic conductivity facilitated Zn^{2+} migration across the interface layer.[16] These combined effects effectively mitigated localized concentration polarization, reduced nucleation energy barriers, offered 3D diffusion of Zn^{2+}, and thus achieved uniform electrical/ionic field distribution on Zn anodes. We then simulated the distribution of stress and strain fields associated with the dendrite growth process on the surfaces of Zn anodes to investigate the suppressing effect on zinc dendrites endowed by the robust mechanical properties of the MXene-CNF_L hydrogel interface layers. The surfaces of bare Zn displayed a lower stress distribution and sharp dendrite growth, as observed from the stress−strain field distribution, due to the absence of stress confinement (Figures 5q, S27a, and S28a). In contrast, the surfaces of the MXene-CNF_L|Zn anodes presented tight stress confinement to suppress dendrite growth (Figures 5r, S27b, and S28b), originating from the high in-plane/out-of-plane elastic modulus of the MXene-CNF_L interface layers (Figure 2f−h and Table S1). The above multifield simulations elaborated that the MXene-CNF_L hydrogel interface layers created more uniform distributions of both the electric field and Zn^{2+} concentration field, and a strong stress confinement field, on the surfaces of Zn anodes, which effectively suppressed dendrite formation, in good agreement with the morphological and phase analysis (Figure 5a−l).

To test the practical application of the MXene-40%CNF_L|Zn anodes in AZIBs, we assembled rechargeable aqueous Zn‖MnO_2 full cells, where the MnO_2 nanorods (Figure S29) synthesized by a simple hydrothermal method,[14] were used as the active cathode material. The as-assembled MXene-40% CNF_L|Zn‖MnO_2 full cells profiled two distinct pairs of redox peaks observed from the CV curves (Figure 6a), corresponding to the insertion/extraction of H^+ and Zn^{2+},[68] and delivered high discharge specific capacities from 323 mAh g^{-1} to 119 mAh g^{-1} at the range of current densities from 0.2 A g^{-1} to 3 A g^{-1} (Figures 6b and S30a), which were higher than those of bare Zn‖MnO_2 full cells of 276 mAh g^{-1} and 96 mAh g^{-1} at the corresponding current densities (Figure S30b). The MXene-40%CNF_L|Zn‖MnO_2 also showed a high-rate capability with a 78.6% capacity retention ratio when the current density returned to 0.2 A g^{-1} (Figure 6b). The results were further supported by EIS measurements (Figure 6d), where MXene-40%CNF_L|Zn‖MnO_2 cells presented a charge transfer resistance (R_{ct}) of 2.5 Ω, significantly lower than that of bare Zn‖MnO_2 (61 Ω), indicating enhanced interface reaction kinetics at the electrode/electrolyte interfaces after the incorporation of the MXene-CNF hydrogel interface layers on Zn anodes. The self-discharge tests (Figure 6c) depicted that the MXene-40%CNF_L|Zn‖MnO_2 maintained 92.8% charging capacity after resting for 24 h, while the bare Zn‖MnO_2 full cells only had 88.4% under the same conditions. This improved capacity retention suggested that the MXene-CNF interface layers can inhibit self-discharge behaviors, probably owing to the inhibition of side reactions on the Zn anodes, as supported by the XRD results (Figure 5l). Figure 6e shows that the MXene-CNF_L hydrogel interface layers also enhanced the cycling stability of full cells, where the MXene-40%CNF_L|Zn‖MnO_2 retained a higher capacity of 67 mAh g^{-1} at a high current density of 3 A g^{-1} after 2000 cycles, compared to the bare Zn‖MnO_2 with 48 mAh g^{-1}. Meanwhile, MXene-40%CNF_L|Zn‖MnO_2 cells always held a CE of above 99% during the 2000 cycles, further indicating high reversibility and stability, which was corroborated by the digital and SEM images of MXene-40%CNF_L|Zn anodes before and after cycling (Figure 6f−k). After 2000 cycles, the MXene-40% CNF_L|Zn anodes displayed much smoother surfaces than bare Zn anodes that had many sharp dendrites compared with the initial Zn foils, mainly because of the multieffects induced by the MXene-CNF hydrogel interface layers, which suppressed the formation of zinc dendrites (Figure 5m−r).

We further explored the versatile application of the MXene-40%CNF_L|Zn anodes in different AZIBs by assembling Zn‖V_2O_5 full cells, where the commercial V_2O_5 was used as intercalation-type cathodes (Figure S31).[13] The CV profiles of the as-assembled MXene-40%CNF_L|Zn‖V_2O_5 cells displayed a pair of redox peaks similar to bare Zn‖V_2O_5 (Figure S32), suggesting the successful Zn^{2+} intercalation and deintercalation process.[8,13] The EIS (Figure 6l) highlighted that the MXene-40%CNF_L|Zn‖V_2O_5 cells presented significantly enhanced charge-transfer kinetics with a much smaller R_{ct} of 90 Ω than the bare Zn‖V_2O_5 (519 Ω), consistent with the results of MXene-40%CNF_L|Zn‖MnO_2 cells. We also evaluated the rate capability (Figure S33) and cyclic stability (Figure 6m) of the Zn‖V_2O_5 cells. Interestingly, the MXene-40%CNF_L|Zn‖V_2O_5 cells exhibited the highest discharging specific capacity of 263 mAh g^{-1} at the 330th cycle at a current density of 2 A g^{-1} after a charging/discharging activation process, which was superior to the highest value of the bare Zn‖V_2O_5 cells of 189 mAh g^{-1} at the 240th cycle. The MXene-40%CNF_L|Zn‖V_2O_5 cells also showed a higher cyclic stability of 103 mAh g^{-1} after 2000 cycles compared with bare Zn‖V_2O_5 cells.

CONCLUSION

In this work, we developed a strategy to fabricate mechanically robust MXene-CNF_L ionotronic hydrogel films, where the building blocks of 1D high-aspect-ratio CNF_L and 2D $Ti_3C_2T_x$ MXene nanosheets were first mixed into stable colloidal codispersions used to assemble the MXene-CNF_L films and the as-assembled films then were post-cross-linked by Zn^{2+} from $ZnSO_4$ solution. We systematically evaluated the toughening effect of the aspect ratio, contents, and cross-linking networks of CNF for the MXene-CNF_L hydrogel films. The optimized MXene-CNF_L hydrogel films presented integrated multifunctionalities, including a high toughness of 18.39 MJ m^{-3}, high strength of 51.30 MPa at an elongation to break of 53.07%, high in-plane elastic modulus of 4.15 GPa, out-of-plane elastic modulus of 3.65 GPa, and mixed electronic/ionic (ionotronic) conductivity of 1.53 S cm^{-1} and 0.52 mS cm^{-1}. The mechanically robust MXene-CNF_L ionotronic hydrogel films also had high zincophilicity with a high binding energy of 1.33 eV and a low migration energy barrier of 0.24 eV for Zn^{2+}. The above multifunctional integrity endowed the capability of MXene-CNF_L hydrogel films as interface layers for stabilizing Zn anodes in AZIBs. More interestingly, the MXene-CNF_L hydrogel interface layers can suppress the corrosion reaction and HER on Zn anodes, reducing the formation of byproducts and extending the electrochemical voltage window and cycle life of the Zn anodes. The symmetrical cells of MXene-40% CNF_L|Zn‖MXene-40%CNF_L|Zn delivered a lower nucleation overpotential of 19 mV, a lower voltage hysteresis of 37 mV, a longer cycle life of over 2700 h, and much more uniform Zn deposition observed from their morphological analysis compared with those of bare Zn||bare Zn cells. Finite element calculations further supported the experimental results. MXene-CNF$_L$ hydrogel interface layers offered strong stress confinement effects and uniform ionic and electronic field distributions on the Zn anodes, effectively suppressing dendrite growth. Additionally, the assembled practical MXene-40% CNF$_L$|Zn||MnO$_2$ full cells presented a sufficiently low charge transfer resistance of 2.50 Ω and a high discharge specific capacity of 323 mAh g^{-1} at 0.2 A g^{-1}, compared with those of the bare Zn||MnO$_2$ cells. Developing mechanically robust MXene-CNF ionotronic hydrogel films as artificial interface layers for Zn anodes can modulate the field distributions of strain−stress, electrons, and zinc ions on Zn anodes, thus suppressing Zn dendrite growth and substantially prolonging the cycle life of AZIBs.

METHODS

Fabrication of CNF. The carboxymethylated CNF was fabricated according to our previous work.[20,69] Briefly, the never-dried sulfite pulp from Nordic Paper AB, Sweden, used as the starting material for the CNF$_L$, was subjected to mechanical beating and then suspended in deionized water. The fibers were solvent exchanged to ethanol four times and were then immersed in a solution of monochloroacetic acid in isopropanol for 30 min. This suspension was then mixed with a solution of NaOH in methanol, which started the carboxymethylation reaction in preheated isopropanol within a reaction vessel equipped with a condenser under stirring for 60 min. The carboxymethylated fibers were then washed with Milli-Q water, 0.01 M HCl, and Milli-Q water sequentially. The carboxymethylated pulp fibers, dispersed in Milli-Q water at 1 wt %, were homogenized through 400 μm/200 μm chambers in series at a pressure of 1000 bar by using a Microfluidics MH-110 homogenizer and three times using 200 μm/100 μm chambers in series at a pressure of 1650 bar. The obtained CNF gel was subsequently diluted with Milli-Q water to prepare the colloidal CNF dispersion. A never-dried sulfite softwood pulp from Domsjö Fabriker AB, Sweden, was used as the starting material for the CNF$_S$, and the process of carboxymethylated reaction was the same for CNF$_L$.

Fabrication of Ti$_3$C$_2$T$_x$ MXene. Ti$_3$C$_2$T$_x$ MXene nanosheets were fabricated based on our previous work.[26] Briefly, 1.6 g of lithium fluoride (LiF) powder was gradually added to 20 mL of 9 M HCl in a 60 mL high-density polyethylene (HDPE) bottle. The mixture was magnetically stirred with a polytetrafluoroethylene (PTFE)-coated magneton stir bar at 300 rpm for 20 min under 35 °C to completely dissolve LiF and *in situ* formed hydrofluoric acid as the etching solution. Then, 1 g Ti$_3$AlC$_2$ powder (<38 μm) was added to the prepared etching solution in an ice bath. After that, this mixed solution was reacted for 2 days under magnetic stirring at 300 rpm under 35 °C. Subsequently, the produced MXene multilayers were washed with deionized water at least 6 times until the pH of the supernatant was above 6. Afterward, the obtained sediment was dispersed into 100 mL of deionized water and delaminated under probe ultrasonic treatment for 90 min (4 s/2 s pulse) under ice bath conditions. Finally, the sonicated solution was centrifuged at 3,500 rpm for 30 min to collect the supernatant as MXene dispersion.

Preparation of MXene-CNF|Zn Anodes. The MXene/CNF codispersion was prepared by mixing the 5 g L^{-1} MXene dispersion and the 1 g L^{-1} CNF dispersion with different content ratios, with a total dry weight of 25 mg, into a centrifuge tube with a total volume of 30 mL by adding additional deionized water and vigorously shaking them to disperse homogeneously. Subsequently, the MXene-CNF composite films were prepared via vacuum filtration using a polyvinylidene fluoride (PVDF) filter membrane with a pore size of 0.45 μm, followed by vacuum drying under a pressure of −0.1 bar for 30 min at 93 °C. Finally, the free-standing MXene-CNF composite films, peeled from the PVDF filters, underwent post-cross-linking by immersing the dry films into 2 M ZnSO$_4$ for 24 h and were synchronously transformed into MXene-CNF hydrogel films. The MXene-CNF|Zn anode was prepared by placing MXene-CNF hydrogel films on the Zn foils and hot-pressing them under vacuum. The commercial Zn foils were pretreated with 0.5 M HCl solution to remove ZnO from the surfaces before assembling the MXene-CNF|Zn electrodes.

Preparation of MnO$_2$ Cathode. The α-MnO$_2$ was synthesized by a reported method.[14] First, 3 mmol MnSO$_4$·H$_2$O and 2 mL of 0.5 M H$_2$SO$_4$ were dissolved in 60 mL of deionized water, followed by magnetic stirring for 10 min. Subsequently, 20 mL of 0.1 M KMnO$_4$ was added to the above solution under magnetic stirring coupled with bath sonication for 1 h. Then, the mixed solution was poured into a Teflon-lined autoclave and reacted at 120 °C for 12 h. Finally, the sediment was washed with deionized water and freeze-dried for 48 h. The obtained α-MnO$_2$ powder was mixed with Super P and PVDF with a mass ratio of 6:3:1 in 1-methyl-2-pyrrolidone (NMP). The above slurry was then coated onto Ti foil, which was dried at 60 °C for 12 h. The coated Ti foil was punched into 12 mm discs and directly utilized as the cathode of Zn||MnO$_2$ full cells.

Preparation of V$_2$O$_5$ Cathode. The V$_2$O$_5$ cathode was prepared by homogeneously mixing commercial V$_2$O$_5$, Super P, and PVDF in a mass ratio of 7:2:1 in NMP. The as-prepared slurry was then uniformly coated onto Ti foil. Subsequently, it was dried in a vacuum oven at 60 °C for 12 h and punched into 12 mm discs, which were directly utilized as the cathode for Zn||V$_2$O$_5$ full cells.

Ionic Conductivity Measurement. The MXene-CNF hydrogel films were sandwiched between two pieces of stainless steel (SS) (D = 5 mm) and assembled into coin cells. The ionic conductivity was tested by EIS measurement using a CHI760E with a frequency range from 200 Hz to 1 MHz and an amplitude of 10 mV around the open-circuit voltage. The ionic conductivity value (mS cm^{-1}) was calculated according to eq 1:

$$\sigma = \frac{d}{R \times S} \tag{1}$$

where d is the thickness of the hydrogel films, R is the resistance at the intercept on the real axis of the Nyquist plot, and S is the working area of the SS.

Electronic Conductivity Measurement. The electronic conductivity of MXene-CNF hydrogel films was tested by using a four-point probe technique on a Keithley 2450. The composite films were cut into 5 × 5 mm small slices, and the four probes contacted the film surface side by side. Electrical conductivity (S m^{-1}) was calculated according to eq 2:

$$\sigma = \frac{1}{R_s \times d} \tag{2}$$

where R_s (Ω sq^{-1}) is the measured sheet resistance, and d is the thickness of the MXene-CNF hydrogel films.

Tensile Stress−Strain Measurement. The tensile stress−strain curve was tested on a universal testing machine (F105IM, Mark-10) at a tensile velocity of 1 mm min^{-1}. The MXene-CNF hydrogel films were cut into strips with a width of 2 mm and a length of about 10 mm, which were then fixed by a homemade clamp. Young's modulus and toughness along the plane were obtained by fitting the slope of the elastic deformation region and integrating the tensile stress−strain curves, respectively.

AFM Indentation Measurement. The out-of-plane Young's modulus of the MXene-CNF hydrogel films was measured by using AFM indentation (Bruker Dimension Icon). Surface morphology and force curves were analyzed by using DNP-10 and RTESPA-525−30 probes, respectively. The elastic constant for force curve measurements was set to 200 N m^{-1}.

Other Characterizations. SEM images were acquired by using a field emission scanning electron microscope (ZEISS Gemini300). XRD patterns were obtained with a Bruker D8 Advance diffractometer. XPS results were gathered with a Thermo Scientific K-Alpha instrument. Fourier transform infrared (FT-IR) spectra were measured on a Thermo Fisher Scientific Nicolet iS20 spectrometer. The AFM images were obtained with a Multimode 8 atomic force microscope (Bruker) in ScanAsyst mode. *In situ* optical microscopy examination was carried out by using a digital microscope (AM7115MZT). Contact angle measurements were conducted on a contact angle meter (JC2000DM).

Electrochemical Measurements. The Zn||Zn symmetrical cells, Zn||Cu half cells, and Zn||MnO_2 full cells were assembled in CR2032-type coin cells and measured using a Neware battery test system (CT-4008Tn-5 V50 mA-HWX). The electrode, electrolyte, and separator of Zn||Zn symmetrical cells are bare Zn or an MXene-CNF|Zn electrode, 2 M $ZnSO_4$, and glass fiber (Whatman GF/A), respectively. The Zn||Cu half cells are assembled by replacing the electrode in the cathode of Zn||Zn symmetrical cells with Cu foil. The Zn||MnO_2 full cells were assembled using the as-prepared MnO_2 cathode, glass fiber separator, 2 M $ZnSO_4$ + 0.1 M $MnSO_4$ electrolyte, and bare Zn or MXene-CNF|Zn anode, respectively. The Zn||V_2O_5 full cells were assembled by using a V_2O_5 cathode, glass fiber separator, 2 M $ZnSO_4$ electrolyte, and bare Zn or MXene-CNF|Zn anode, respectively. CV, EIS, and LSV were measured on the CHI760E electrochemical workstation. The EIS measurement was conducted on a frequency range of 10^6 to 10^{-2} Hz with a potential amplitude of 5 mV. The Tafel curve was measured by a three-electrode system with bare Zn or MXene-CNF|Zn electrode as the working electrode, Pt as the counter electrode, and Ag/AgCl as the reference electrode, respectively.

Density Functional Theory (DFT) Calculations. We employed the Vienna Ab Initio Simulation Package (VASP) to perform all density functional theory (DFT) calculations within the generalized gradient approximation (GGA) using the PBE formulation. We chose the projected augmented wave (PAW) potentials to describe the ionic cores and to take valence electrons into account using a plane wave basis set with a kinetic energy cutoff of 400 eV. Partial occupancies of the Kohn−Sham orbitals were allowed using the Gaussian smearing method and a width of 0.05 eV. The electronic energy was considered self-consistent when the energy change was smaller than 10^{-5} eV. A geometry optimization was considered to be convergent when the force change was smaller than 0.02 eV/Å.

Grimme's DFT-D3 methodology was used to describe the dispersion interactions. The adsorption energy (E_{ads}) of a Zn single atom was defined as

$$E_{\mathrm{ads}} = E_{\mathrm{Zn/surf}} - E_{\mathrm{surf}} - E_{\mathrm{Zn}} \tag{3}$$

where $E_{\mathrm{Zn/surf}}$, E_{surf}, and E_{Zn} are the energy of the adsorbate Zn adsorbed on the surface, the energy of a clean surface, and the energy of one Zn atom, respectively. Finally, transition states for elementary reaction steps were determined by the nudged elastic band (NEB) method, where the path between the reactant and product was discretized into a series of structural images.

Finite Element Calculation. The model for finite element calculations was coupled with the third-order current distribution module and the level set module of COMSOL 6.0 to simulate the electrochemical behaviors of Zn^{2+}. The Zn^{2+} was first transferred from the electrolyte to the zinc metal surface and then reduced to Zn atoms, which were further deposited on the substrate surface. There were two main processes involved:

1. Mass transport is described by the Nernst−Planck equation:

$$N_{\mathrm{Zn}^{2+}} = -D_{\mathrm{Zn}^{2+}}\left(\nabla c_{\mathrm{Zn}^{2+}} + \frac{zFc_{\mathrm{Zn}^{2+}}}{RT}\nabla \varphi_1\right) \tag{4}$$

2. Charge transfer is described by the Butler−Volmer equation:

$$i = i_0\left(\exp\left(\frac{\partial_{\mathrm{a}}F\eta_a}{RT}\right) - \exp\left(\frac{\partial_{\mathrm{c}}F\eta_c}{RT}\right)\right) \tag{5}$$

A transient simulation of the deposition system, with or without an MXene-CNF film, was performed. The diffusion of the ion concentration followed the Nernst−Planck equation, and the reaction at the electrode surface followed the Butler−Volmer equation. To reduce computational complexity and simplify the actual system, a model domain with a length of 60 μm and a height of 50 μm was constructed. A projection at the bottom was set to represent the Zn surface, and an MXene-CNF film domain with a height of 8 μm was set. The initial boundary potential and external potential were set to 0.2 and 0 V, respectively. The top cathode region and the boundary on both sides were defined as the undeformed boundary, and the bottom anode boundary was set as the deformed electrode surface.

The stress field distribution during the dendritic formation process on the Zn anode was further determined through a COMSOL simulation for enhanced computational analysis. During the electrochemical reaction process, Zn^{2+} was driven by the electric field and eventually deposited onto the surface of the anodes, forming Zn dendrites. Given that the phase-field method can accurately describe the complex variations of the phase interface in two-phase flow calculations, the phase-field equation was adopted to simulate the growth of zinc dendrites. By adjustment of the elastic modulus of the MXene-CNF films, the morphology of the dendrites can be further regulated. In this model, as the phase-field order parameter was a nonconservative quantity, the Allen-Cahn form of the phase-field equation was employed:

$$\frac{\partial \varphi}{\partial t} = -L_i\left[\frac{\partial g(\varphi)}{\partial \varphi} - \kappa \nabla^2 \varphi\right] - L_m h'(\varphi)\left\{e^{\left[\frac{(1-\alpha)nFP}{RT}\right]} - \frac{c_+}{c_0} e^{\left[\frac{-\alpha nFP}{RT}\right]}\right\} \tag{6}$$

where φ is the phase field sequence parameter, the φ value in the electrode phase is 1, but φ in the electrolyte phase is 0, and φ varied continuously from 0 to 1 in the electrode−electrolyte intermediate phase. L_i and L_m are the interface mobility and reaction coefficient, respectively. $g(\varphi) = W\varphi^2(1-\varphi)^2$ is a two-well function. $h(\varphi) = \varphi^2\ (6\varphi^2-15\varphi + 10)$ is an interpolation function. R, T, n, and F are the gas constant, temperature, number of transferred electrons, and Faraday's constant, respectively.

In the phase-field equation, φ was coupled with Zn^{2+} concentration (c) and overpotential (P). To simulate the spatiotemporal distribution of Zn^{2+} concentration, the Nernst−Planck equation was used:

$$\frac{\partial c^+}{\partial t} = \nabla \cdot \left(D_{\mathrm{eff}} \nabla c^+ - \frac{D_{\mathrm{eff}} nf}{RT} \nabla P\right) - c\frac{\partial \varphi}{\partial t} \tag{7}$$

where D_{eff} is the effective diffusivity, expressed as $D_e \times h(\varphi) + D_l \times [1-h(\varphi)]$, in which D_e and D_l are the diffusivity of Zn^{2+} in the electrode and electrolyte, respectively. In addition, Poisson's equation was used to ensure the electric neutrality of the calculated system, and the distribution and evolution of the electric potential are expressed:

$$\nabla \cdot \sigma_{\mathrm{eff}} \nabla P = nFc\frac{\partial \varphi}{\partial t} \tag{8}$$

Where σ_{eff} is the effective conductivity, written as $\sigma_e \times h(\varphi) + \sigma_l \times [1-h(\varphi)]$, where σ_e and σ_l correspond to the conductivity of Zn^{2+} in the electrode and electrolyte, respectively. The above-governing equations were solved instantaneously using the Partial Differential Equation (PDE) module in COMSOL Multiphysics 6.2.

ASSOCIATED CONTENT

Supporting Information

The Supporting Information is available free of charge at https://pubs.acs.org/doi/10.1021/acsnano.5c01497.

> Size distribution of CNF and MXene (Figure S1); optical photo and SEM image of MXene-40%CNF_L film (Figure S2); stress−strain curves of MXene-CNF film in a dry state (Figure S3); AFM height image of MXene-40%CNF_L film (Figure S4); AFM peak-force-error image and corresponding height image of MXene-40% CNF_S film (Figure S5); optical photos after bath ultrasonication (Figure S6); SEM images of fracture morphologies for MXene-CNF_L hydrogel film (Figure S7); XPS spectra of MXene-40%CNF_L films (Figure S8); FT-IR patterns of MXene-40%CNF_L films (Figure S9); schematic illustration of Zn^{2+} cross-linking effect (Figure S10); AFM indentation profiles (Figure S11, S12); water contact angles (Figure S13); Nyquist plots of the MXene-CNF hydrogel films (Figure S14); nucleation overpotential profiles of Zn||Zn cells (Figures S15, S16); CV curves of Zn||Cu cells (Figure S17); DFT calculation models of the Zn^{2+} transport path (Figure S18); oxygen evolution potential (Figure S19); LSV curve of MXene-40%CNF_S|Zn anode (Figure S20); rate performance of MXene-40%CNF_S|Zn symmetrical cells (Figure S21); cycling performance profiles (Figure S22); schematic illustration of zinc deposition behaviors (Figure S23); XRD patterns (Figure S24); finite element calculation of electric field distribution (Figure S25); finite element calculation of Zn^{2+} concentration distribution (Figure S26); finite element calculation of stress field distribution (Figure S27); finite element calculation of dendrite morphology evolutions (Figure S28); SEM images and XRD pattern of MnO_2 (Figure S29); galvanostatic charge/discharge profiles (Figure S30); SEM images and XRD pattern of V_2O_5 (Figure S31); CV curves of Zn||V_2O_5 full cells (Figure S32); galvanostatic charge/discharge profiles of Zn||V_2O_5 full cells (Figure S33); electromechanical properties of MXene-CNF_L ionotronic hydrogel films (Table S1); mechanical properties of previously reported hydrogels (Table S2); content of the functional groups from XPS O 1s spectrum (Table S3); ionotronic properties compared with previously reported hydrogels (Table S4) (PDF)

AUTHOR INFORMATION

Corresponding Authors

Liming Zhang − *College of Textile and Clothing, Qingdao University, Qingdao 266071, China;*
Email: zhangliminglz@qdu.edu.cn

Huanlei Wang − *School of Materials Science and Engineering, Ocean University of China, Qingdao 266100, China; Qigndao Key Laboratory of Marine Extreme Environment Materials, Ocean University of China, Qingdao 266100, China;* orcid.org/0000-0001-8218-1762;
Email: huanleiwang@ouc.edu.cn

Mahiar Max Hamedi − *Department of Fibre and Polymer Technology, Wallenberg Wood Science Center, KTH Royal Institute of Technology, Stockholm SE-100 44, Sweden;* orcid.org/0000-0001-9088-1064; Email: mahiar@kth.se

Feng Xu − *State Key Laboratory of Efficient Production of Forest Resources, Beijing Key Laboratory of Lignocellulosic Chemistry, Beijing Forestry University, Beijing 100083, China*; Email: xfx315@bjfu.edu.cn

Weiqian Tian − *School of Materials Science and Engineering, Ocean University of China, Qingdao 266100, China; Qigndao Key Laboratory of Marine Extreme Environment Materials, Ocean University of China, Qingdao 266100, China;* orcid.org/0000-0003-3497-2054;
Email: tianweiqian@ouc.edu.cn

Authors

Mengyu Liu − *School of Materials Science and Engineering, Ocean University of China, Qingdao 266100, China*

Jowan Rostami − *Department of Fibre and Polymer Technology, Wallenberg Wood Science Center, KTH Royal Institute of Technology, Stockholm SE-100 44, Sweden*

Teng Zhang − *A.J. Drexel Nanomaterials Institute and Department of Materials Science and Engineering, Drexel University, Philadelphia, Pennsylvania 19104, United States;* orcid.org/0000-0002-4939-0594

Kyle Matthews − *A.J. Drexel Nanomaterials Institute and Department of Materials Science and Engineering, Drexel University, Philadelphia, Pennsylvania 19104, United States*

Sheng Chen − *State Key Laboratory of Efficient Production of Forest Resources, Beijing Key Laboratory of Lignocellulosic*

Chemistry, Beijing Forestry University, Beijing 100083, China; orcid.org/0000-0001-6094-3084
Wenjie Fan – *School of Materials Science and Engineering, Ocean University of China, Qingdao 266100, China*
Yue Zhu – *School of Materials Science and Engineering, Ocean University of China, Qingdao 266100, China*
Jingwei Chen – *School of Materials Science and Engineering, Ocean University of China, Qingdao 266100, China;* orcid.org/0000-0003-4440-400X
Minghua Huang – *School of Materials Science and Engineering, Ocean University of China, Qingdao 266100, China;* orcid.org/0000-0002-9622-3131
Jingyi Wu – *School of Materials Science and Engineering, Ocean University of China, Qingdao 266100, China;* orcid.org/0000-0001-5344-2652
Lars Wågberg – *Department of Fibre and Polymer Technology, Wallenberg Wood Science Center, KTH Royal Institute of Technology, Stockholm SE-100 44, Sweden*
Yury Gogotsi – *A.J. Drexel Nanomaterials Institute and Department of Materials Science and Engineering, Drexel University, Philadelphia, Pennsylvania 19104, United States;* orcid.org/0000-0001-9423-4032

Complete contact information is available at:
https://pubs.acs.org/10.1021/acsnano.5c01497

Author Contributions

M.L. and W.T. conceived the idea and methodology, and wrote the initial draft of the manuscript. M.L. conducted most of the experiments and data collection under the supervision of W.T., L.W., and Y.G. worked on the discussion and revised the original manuscript. J.R., T.Z., and K.M. worked on material preparation. W.T., F.X., M.M., H.W., and L.Z. contributed to the supervision and funding of the work. All authors worked on the data analysis, discussion, and writing.

Notes

The authors declare no competing financial interest.

ACKNOWLEDGMENTS

W.T., L.Z., and H.W. acknowledge funding from the National Natural Science Foundation of China (No. 52203341, 32301532, 22179123), the Shandong Excellent Young Scientists Fund Program (Overseas) (No. 2023HWYQ-061), the Taishan Scholar Program of Shandong Province, China (No. tsqn202306105, tsqn202211048), the Shandong Province Natural Science Foundation (No. ZR2023QC097), the Major Basic Research Projects of the Shandong Natural Science Foundation (ZR2024ZD37), and the Fundamental Research Funds for the Central Universities (No. 202312011). F.X. acknowledges funding from the National Natural Science Foundation of China (No. U22A20422) and the Program of Introducing Talents of Discipline to Universities, Project 111 (Grant No. B21022). M.H. acknowledges funding from the Swedish Research Council (No. 2021–03882). Y.G. acknowledges the Fluid Interface Reactions, Structures, and Transport (FIRST) Center, an Energy Frontier Research Center funded by the U.S. Department of Energy, Office of Science, Office of Basic Energy Sciences.

REFERENCES

(1) Jang, J.; Chun, J.; Jo, C. Biopolymer-Blended Protective Layer for Use in Stabilizing the Zinc Anode in Metal Battery Applications. *Energy Storage Mater.* **2023**, *62*, 102948.

(2) He, H.; Qin, H.; Wu, J.; Chen, X.; Huang, R.; Shen, F.; Wu, Z.; Chen, G.; Yin, S.; Liu, J. Engineering Interfacial Layers to Enable Zn Metal Anodes for Aqueous Zinc-Ion Batteries. *Energy Storage Mater.* **2021**, *43*, 317–336.

(3) Zhang, H.; Gan, X.; Yan, Y.; Zhou, J. A Sustainable Dual Cross-Linked Cellulose Hydrogel Electrolyte for High-Performance Zinc-Metal Batteries. *Nano-Micro Lett.* **2024**, *16*, 106.

(4) Yu, L.; Huang, J.; Wang, S.; Qi, L.; Wang, S.; Chen, C. Ionic Liquid "Water Pocket" for Stable and Environment-Adaptable Aqueous Zinc Metal Batteries. *Adv. Mater.* **2023**, *35*, 2210789.

(5) Liu, H.; Wang, J.-G.; You, Z.; Wei, C.; Kang, F.; Wei, B. Rechargeable Aqueous Zinc-Ion Batteries: Mechanism, Design Strategies and Future Perspectives. *Mater. Today* **2021**, *42*, 73–98.

(6) Zhang, F.; Meng, Q.; Qian, J. W.; Chen, J.; Dong, W. X.; Chen, K.; Cui, Y. F.; Dou, S. X.; Chen, L. F. Selective Interface Engineering with Large Π-Conjugated Molecules Enables Durable Zn Anodes. *Angew. Chem., Int. Ed.* **2025**, No. e202425487.

(7) Han, L.; Guo, Y.; Ning, F.; Liu, X.; Yi, J.; Luo, Q.; Qu, B.; Yue, J.; Lu, Y.; Li, Q. Lotus Effect Inspired Hydrophobic Strategy for Stable Zn Metal Anodes. *Adv. Mater.* **2024**, *36*, 2308086.

(8) Zhao, Z.; Zhao, J.; Hu, Z.; Li, J.; Li, J.; Zhang, Y.; Wang, C.; Cui, G. Long-Life and Deeply Rechargeable Aqueous Zn Anodes Enabled by a Multifunctional Brightener-Inspired Interphase. *Energ Environ. Sci.* **2019**, *12*, 1938–1949.

(9) Yang, S.; Zhang, Y.; Zhang, Y.; Deng, J.; Chen, N.; Xie, S.; Ma, Y.; Wang, Z. Designing Anti-Swelling Nanocellulose Separators with Stable and Fast Ion Transport Channels for Efficient Aqueous Zinc-Ion Batteries. *Adv. Funct. Mater.* **2023**, *33*, 2304280.

(10) Du, W.; Ang, E. H.; Yang, Y.; Zhang, Y.; Ye, M.; Li, C. C. Challenges in the Material and Structural Design of Zinc Anode Towards High-Performance Aqueous Zinc-Ion Batteries. *Energ Environ. Sci.* **2020**, *13*, 3330–3360.

(11) Guo, X.; He, G. Opportunities and Challenges of Zinc Anodes in Rechargeable Aqueous Batteries. *J. Mater. Chem. A* **2023**, *11*, 11987–12001.

(12) Zheng, Z.; Guo, S.; Yan, M.; Luo, Y.; Cao, F. A Functional Janus Ag Nanowires/Bacterial Cellulose Separator for High-Performance Dendrite-Free Zinc Anode under Harsh Conditions. *Adv. Mater.* **2023**, *35*, 2304667.

(13) Fan, W.; Li, P.; Shi, J.; Chen, J.; Tian, W.; Wang, H.; Wu, J.; Yu, G. Atomic Zincophilic Sites Regulating Microspace Electric Fields for Dendrite-Free Zinc Anode. *Adv. Mater.* **2024**, *36*, 2307219.

(14) Cui, Y.; Chen, W.; Xin, W.; Ling, H.; Hu, Y.; Zhang, Z.; He, X.; Zhao, Y.; Kong, X. Y.; Wen, L.; et al. Gradient Quasi-Solid Electrolyte Enables Selective and Fast Ion Transport for Robust Aqueous Zinc-Ion Batteries. *Adv. Mater* **2024**, *36*, 2308639.

(15) Liu, C.; Li, Z.; Zhang, X.; Xu, W.; Chen, W.; Zhao, K.; Wang, Y.; Hong, S.; Wu, Q.; Li, M. C.; et al. Synergic Effect of Dendrite-Free and Zinc Gating in Lignin-Containing Cellulose Nanofibers-MXene Layer Enabling Long-Cycle-Life Zinc Metal Batteries. *Adv. Sci.* **2022**, *9*, 2202380.

(16) Hong, L.; Wu, X.; Liu, Y. S.; Yu, C.; Liu, Y.; Sun, K.; Shen, C.; Huang, W.; Zhou, Y.; Chen, J. S.; et al. Self-Adapting and Self-Healing Hydrogel Interface with Fast Zn^{2+} Transport Kinetics for Highly Reversible Zn Anodes. *Adv. Funct. Mater.* **2023**, *33*, 2300952.

(17) Zhang, Y. Z.; Cao, Z. J.; Liu, S. J.; Du, Z. G.; Cui, Y. L.; Gu, J. N.; Shi, Y. Z.; Li, B.; Yang, S. B. Charge-Enriched Strategy Based on MXene-Based Polypyrrole Layers toward Dendrite-Free Zinc Metal Anodes. *Adv. Energy Mater.* **2022**, *12*, 2103979.

(18) Cai, X.; Wang, X.; Bie, Z.; Jiao, Z.; Li, Y.; Yan, W.; Fan, H. J.; Song, W. A Layer-by-Layer Self-Assembled Biomacromolecule Film for Stable Zinc Anode. *Adv. Mater.* **2024**, *36*, 2306734.

(19) Xu, W.; Liao, X.; Xu, W.; Zhao, K.; Yao, G.; Wu, Q. Ion Selective and Water Resistant Cellulose Nanofiber/MXene Membrane Enabled Cycling Zn Anode at High Currents. *Adv. Energy Mater.* **2023**, *13*, 2300283.

(20) Li, L.; Tian, W.; VahidMohammadi, A.; Rostami, J.; Chen, B.; Matthews, K.; Ram, F.; Pettersson, T.; Wågberg, L.; Benselfelt, T.;

et al. Ultrastrong Ionotronic Films Showing Electrochemical Osmotic Actuation. *Adv. Mater.* **2023**, *35*, 2301163.

(21) Cao, W.-T.; Chen, F.-F.; Zhu, Y.-J.; Zhang, Y.-G.; Jiang, Y.-Y.; Ma, M.-G.; Chen, F. Binary Strengthening and Toughening of MXene/Cellulose Nanofiber Composite Paper with Nacre-Inspired Structure and Superior Electromagnetic Interference Shielding Properties. *ACS Nano* **2018**, *12*, 4583−4593.

(22) Zhou, Z.; Song, Q.; Huang, B.; Feng, S.; Lu, C. Facile Fabrication of Densely Packed Ti_3C_2 MXene/Nanocellulose Composite Films for Enhancing Electromagnetic Interference Shielding and Electro-/Photothermal Performance. *ACS Nano* **2021**, *15*, 12405−12417.

(23) Tian, W.; VahidMohammadi, A.; Reid, M. S.; Wang, Z.; Ouyang, L.; Erlandsson, J.; Pettersson, T.; Wagberg, L.; Beidaghi, M.; Hamedi, M. M. Multifunctional Nanocomposites with High Strength and Capacitance Using 2D MXene and 1D Nanocellulose. *Adv. Mater.* **2019**, *31*, 1902977.

(24) Chen, Z.; Hu, Y.; Shi, G.; Zhuo, H.; Ali, M. A.; Jamróz, E.; Zhang, H.; Zhong, L.; Peng, X. Advanced Flexible Materials from Nanocellulose. *Adv. Funct. Mater.* **2023**, *33*, 2214245.

(25) Xu, T.; Du, H.; Liu, H.; Liu, W.; Zhang, X.; Si, C.; Liu, P.; Zhang, K. Advanced Nanocellulose-Based Composites for Flexible Functional Energy Storage Devices. *Adv. Mater.* **2021**, *33*, 2101368.

(26) Tian, W.; VahidMohammadi, A.; Wang, Z.; Ouyang, L.; Beidaghi, M.; Hamedi, M. M. Layer-by-Layer Self-Assembly of Pillared Two-Dimensional Multilayers. *Nat. Commun.* **2019**, *10* (1), 2558.

(27) Li, W.; Zhou, T.; Zhang, Z.; Li, L.; Lian, W.; Wang, Y.; Lu, J.; Yan, J.; Wang, H.; Wei, L.; Cheng, Q. Ultrastrong MXene Film Induced by Sequential Bridging with Liquid Metal. *Science* **2024**, *385*, 62−68.

(28) Cao, Z.; Zhu, Y. B.; Chen, K.; Wang, Q.; Li, Y.; Xing, X.; Ru, J.; Meng, L. G.; Shu, J.; Shpigel, N.; et al. Super-Stretchable and High-Energy Micro-Pseudocapacitors Based on MXene Embedded Ag Nanoparticles. *Adv. Mater.* **2024**, *36*, 2401271.

(29) Wan, H.; Chen, Y.; Tao, Y.; Chen, P.; Wang, S.; Jiang, X.; Lu, A. MXene-Mediated Cellulose Conductive Hydrogel with Ultra-stretchability and Self-Healing Ability. *ACS Nano* **2023**, *17*, 20699−20710.

(30) Mohammadi, A. V.; Rosen, J.; Gogotsi, Y. The World of Two-Dimensional Carbides and Nitrides (MXenes). *Science* **2021**, *372*, 1165.

(31) Jing, S.; Wu, L.; Siciliano, A. P.; Chen, C.; Li, T.; Hu, L. The Critical Roles of Water in the Processing, Structure, and Properties of Nanocellulose. *ACS Nano* **2023**, *17*, 22196−22226.

(32) Liang, J.; He, J.; Xin, Y.; Gao, W.; Zeng, G.; He, X. MXene Reinforced PAA/PEDOT: PSS/MXene Conductive Hydrogel for Highly Sensitive Strain Sensors. *Macromol. Mater. Eng.* **2022**, *308*, 2200519.

(33) Xu, W.; Newton, M. A. A.; Chen, Z.; Xin, B. D. Characterization, and Performance Evaluation of Novel PVA/CS/CNF/MOP TN Ionic Conductive Hydrogels for Flexible Sensors. *J. Polym. Sci.* **2024**, *62*, 2744−2761.

(34) Sun, Z.; Dong, C.; Chen, B.; Li, W.; Hu, H.; Zhou, J.; Li, C.; Huang, Z. S. Tough, and Anti-Swelling Supramolecular Conductive Hydrogels for Amphibious Motion Sensors. *Small* **2023**, *19*, 2303612.

(35) Cao, X.; Wu, G.; Li, K.; Hou, C.; Li, Y.; Zhang, Q.; Wang, H. High-Performance Zn^{2+}-Crosslinked MXene Fibers for Versatile Flexible Electronics. *Adv. Funct. Mater.* **2024**, *34*, 2407975.

(36) Zhu, Q.; Chen, X.; Li, D.; Xiao, L.; Chen, J.; Zhou, L.; Chen, J.; Yuan, Q. Large Enhancement on Performance of Flexible Cellulose-Based Piezoelectric Composite Film by Welding CNF and MXene via Growing ZnO to Construct a "Brick-Rebar-Mortar" Structure. *Adv. Funct. Mater.* **2024**, *34*, 2408588.

(37) Zhang, F.; Qian, J.-W.; Dong, W.-X.; Qu, Y.-F.; Chen, K.; Chen, J.; Cui, Y.-F.; Chen, L.-F. Integration of Confinement Crosslinking and *in situ* Grafting for Constructing Artificial Interphases toward Stabilized Zinc Anodes. *Energ Environ. Sci* **2024**, *17*, 7258−7270.

(38) Tie, Z.; Zhang, Y.; Zhu, J.; Bi, S.; Niu, Z. An Air-Rechargeable Zn/Organic Battery with Proton Storage. *J. Am. Chem. Soc.* **2022**, *144*, 10301−10308.

(39) Tian, W.; Gao, Q.; Tan, Y.; Yang, K.; Zhu, L.; Yang, C.; Zhang, H. Bio-Inspired Beehive-Like Hierarchical Nanoporous Carbon Derived from Bamboo-Based Industrial by-Product as a High Performance Supercapacitor Electrode Material. *J. Mater. Chem. A* **2015**, *3*, 5656−5664.

(40) Andrade, G. R. S.; Nascimento, C. C.; Lima, Z. M.; Teixeira-Neto, E.; Costa, L. P.; Gimenez, I. F. Star-Shaped ZnO/Ag Hybrid Nanostructures for Enhanced Photocatalysis and Antibacterial Activity. *Appl. Surf. Sci.* **2017**, *399*, 573−582.

(41) Li, X.; Zhang, J.; Ju, Z.; Li, Y.; Xu, J.; Xin, J.; Lu, X.; Zhang, S. Facile Synthesis of Cellulose/ZnO Aerogel with Uniform and Tunable Nanoparticles Based on Ionic Liquid and Polyhydric Alcohol. ACS Sustain. *Chem. Eng.* **2018**, *6*, 16248−16254.

(42) Benselfelt, T.; Nordenström, M.; Hamedi, M. M.; Wågberg, L. Ion-Induced Assemblies of Highly Anisotropic Nanoparticles Are Governed by Ion−Ion Correlation and Specific Ion Effects. *Nanoscale* **2019**, *11*, 3514−3520.

(43) Benselfelt, T.; Kummer, N.; Nordenström, M.; Fall, A. B.; Nyström, G.; Wågberg, L. The Colloidal Properties of Nanocellulose. *ChemSuschem* **2023**, *16* (8), No. e202201955.

(44) Sellman, F. A.; Rostami, J.; Östmans, R.; Cortes Ruiz, M. F.; Lindström, S. B.; Wågberg, L.; Benselfelt, T. Influence of Fibril Aspect Ratio, Chemical Functionality, and Volume Fraction on the Mechanical Properties of Cellulose Nanofibril Materials. *Cellulose* **2024**, *31*, 8007−8025.

(45) Qu, Y. F.; Qian, J. W.; Zhang, F.; Zhu, Z.; Zhu, Y.; Hou, Z.; Meng, Q.; Chen, K.; Dou, S. X.; Chen, L. F. Constructing 3D Crosslinked Macromolecular Networks as a Highly Efficient Interface Layer for Ultra-Stable Zn Metal Anodes. *Adv. Mater.* **2025**, *37*, 2413370.

(46) Lotfi, R.; Zandi, N.; Pourjavadi, A.; Christiansen, J. D. C.; Gurevich, L.; Mehrali, M.; Dolatshahi-Pirouz, A.; Pennisi, C. P.; Tamjid, E.; Simchi, A. Engineering Photo-Cross-Linkable MXene-Based Hydrogels: Durable Conductive Biomaterials for Electroactive Tissues and Interfaces. *ACS Biomater. Sci. Eng.* **2024**, *10*, 800−813.

(47) Ni, Y.; Zang, X.; Chen, J.; Zhu, T.; Yang, Y.; Huang, J.; Cai, W.; Lai, Y. Flexible MXene-Based Hydrogel Enables Wearable Human-Computer Interaction for Intelligent Underwater Communication and Sensing Rescue. *Adv. Funct. Mater.* **2023**, *33*, 2301127.

(48) Yang, B.; Yuan, W. Highly Stretchable and Transparent Double-Network Hydrogel Ionic Conductors as Flexible Thermal−Mechanical Dual Sensors and Electroluminescent Devices. *ACS Appl. Mater. Interfaces* **2019**, *11*, 16765−16775.

(49) Wang, Y.; Zeng, S.; Shi, S.; Jiang, Y.; Du, Z.; Wang, B.; Li, X. Hybrid Assembly of Conducting Nanofiber Network for Ultra-Stretchable and Highly Sensitive Conductive Hydrogels. *J. Mater. Sci. Technol.* **2024**, *169*, 1−10.

(50) Zha, X.-J.; Zhang, S.-T.; Pu, J.-H.; Zhao, X.; Ke, K.; Bao, R.-Y.; Bai, L.; Liu, Z.-Y.; Yang, M.-B.; Yang, W. Nanofibrillar Poly(Vinyl Alcohol) Ionic Organohydrogels for Smart Contact Lens and Human-Interactive Sensing. *ACS Appl. Mater. Interfaces* **2020**, *12*, 23514−23522.

(51) Xie, J.; Su, F.; Fan, L.; Mu, Z.; Wang, H.; He, Z.; Zhang, W.; Yao, D.; Zheng, Y. Robust and Stretchable $Ti_3C_2T_x$ MXene/PEI Conductive Composite Dual-Network Hydrogels for Ultrasensitive Strain Sensing. *Compos Part A-Appl. S* **2024**, *176*, 107833.

(52) Xu, C.; Guan, S.; Dong, X.; Qi, M. Super Strong Gelatin/Cellulose Nanofiber Hybrid Hydrogels without Covalent Cross-Linking for Strain Sensor and Supercapacitor. *Compos Part A-Appl. S* **2023**, *164*, 107287.

(53) Wang, D.; Zhang, N.; Zhang, Y.; Chang, L.; Tang, H.; Zhang, W.; Zhu, Q. Electric Field Sponge Effect of Conducting Polymer Interphases Boosts the Kinetics and Stability of Zinc Metal Anodes. *Adv. Energy Mater.* **2024**, *15*, 2404090.

(54) Chen, A.; Zhao, C.; Guo, Z.; Lu, X.; Liu, N.; Zhang, Y.; Fan, L.; Zhang, N. Fast-Growing Multifunctional $ZnMoO_4$ Protection Layer

Enable Dendrite-Free and Hydrogen-Suppressed Zn Anode. *Energy Storage Mater.* **2022**, *44*, 353−359.

(55) Zhong, Y.; Cheng, Z.; Zhang, H.; Li, J.; Liu, D.; Liao, Y.; Meng, J.; Shen, Y.; Huang, Y. Monosodium Glutamate, an Effective Electrolyte Additive to Enhance Cycling Performance of Zn Anode in Aqueous Battery. *Nano Energy* **2022**, *98*, 107220.

(56) Zhang, Y.; Yang, S.; Deng, J.; Chen, N.; Xie, S.; Zhou, J.; Wang, Z. Rational Design of Zincophilic Ag/Permselective PEDOT: PSS Heterogeneous Interfaces for High-Rate Zinc Electrodeposition. *Small* **2023**, *19*, 2303665.

(57) Lei, S.-Y.; Feng, J.-X.; Chen, Y.-C.; Zheng, D.; Liu, W.-X.; Shi, W.-H.; Wu, F.-F.; Cao, X.-H. Advance in Reversible Zn Anodes Promoted by 2D Materials. *Rare Met* **2024**, *43*, 1350−1369.

(58) Ye, Y.; Yu, L.; Lizundia, E.; Zhu, Y.; Chen, C.; Jiang, F. Cellulose-Based Ionic Conductor: An Emerging Material toward Sustainable Devices. *Chem. Rev* **2023**, *123*, 9204−9264.

(59) Li, Z.; Robertson, A. W. Electrolyte Engineering Strategies for Regulation of the Zn Metal Anode in Aqueous Zn-Ion Batteries. *Battery Energy* **2023**, *2*, 220029.

(60) Guo, J.; Wang, Y.; Li, S.; Qin, Y.; Meng, Y.; Jiang, L.; Huang, H.; Shen, L. Chitosan Hydrogel Polyelectrolyte-Modified Cotton Pad as Dendrite-Inhibiting Separators for Stable Zinc Anodes in Aqueous Zinc-Ion Batteries. *J. Power Sources* **2023**, *580*, 233392.

(61) Su, Y.; Liu, B.; Zhang, Q.; Peng, J.; Wei, C.; Li, S.; Li, W.; Xue, Z.; Yang, X.; Sun, J. Printing-Scalable $Ti_3C_2T_x$ MXene-Decorated Janus Separator with Expedited Zn^{2+} Flux toward Stabilized Zn Anodes. *Adv. Funct. Mater.* **2022**, *32*, 2204306.

(62) Yang, Q.-H.; Wang, L.-F.; Wang, X.-Y.; Zhen, M.-M. Progress and Challenges of Electrolyte Modulation in Aqueous Zinc-Ion Batteries. *Rare Met* **2024**, *43*, 2940−2967.

(63) Lei, X.; Ma, Z.; Bai, L.; Wang, L.; Ding, Y.; Song, S.; Song, A.; Dong, H.; Tian, H.; Tian, H.; Meng, X.; Liu, H.; Sun, B.; Shao, G.; Wang, G. Porous ZnP Matrix for Long-Lifespan and Dendrite-Free Zn Metal Anodes. *Battery Energy* **2023**, *2*, 230024.

(64) Zhang, T.; Tang, Y.; Guo, S.; Cao, X.; Pan, A.; Fang, G.; Zhou, J.; Liang, S. Fundamentals and Perspectives in Developing Zinc-Ion Battery Electrolytes: A Comprehensive Review. *Energ Environ. Sci.* **2020**, *13*, 4625−4665.

(65) Xiang, Z.; Li, Y.; Cheng, X.; Yang, C.; Wang, K.-P.; Zhang, Q.; Wang, L. Lean-Water Hydrogel Electrolyte with Improved Ion Conductivity for Dendrite-Free Zinc-Ion Batteries. *Chem. Eng. J.* **2024**, *490*, 151524.

(66) Li, X.; Wang, L.; Fu, Y.; Dang, H.; Wang, D.; Ran, F. Optimization Strategies toward Advanced Aqueous Zinc-Ion Batteries: From Facing Key Issues to Viable Solutions. *Nano Energy* **2023**, *116*, 108858.

(67) Zhou, X.; Wen, B.; Cai, Y.; Chen, X.; Li, L.; Zhao, Q.; Chou, S. L.; Li, F. Interfacial Engineering for Oriented Crystal Growth toward Dendrite-Free Zn Anode for Aqueous Zinc Metal Battery. *Angew. Chem., Int. Ed.* **2024**, *63*, No. e202402342.

(68) Zhang, N.; Huang, S.; Yuan, Z.; Zhu, J.; Zhao, Z.; Niu, Z. Direct Self-Assembly of MXene on Zn Anodes for Dendrite-Free Aqueous Zinc-Ion Batteries. *Angew. Chem., Int. Ed.* **2021**, *60*, 2861−2865.

(69) Rostami, J.; Benselfelt, T.; Maddalena, L.; Avci, C.; Sellman, F. A.; Cinar Ciftci, G.; Larsson, P. A.; Carosio, F.; Akhtar, F.; Tian, W.; et al. Shaping 90 wt% NanoMOFs into Robust Multifunctional Aerogels Using Tailored Bio-Based Nanofibrils. *Adv. Mater.* **2022**, *34*, 2204800.

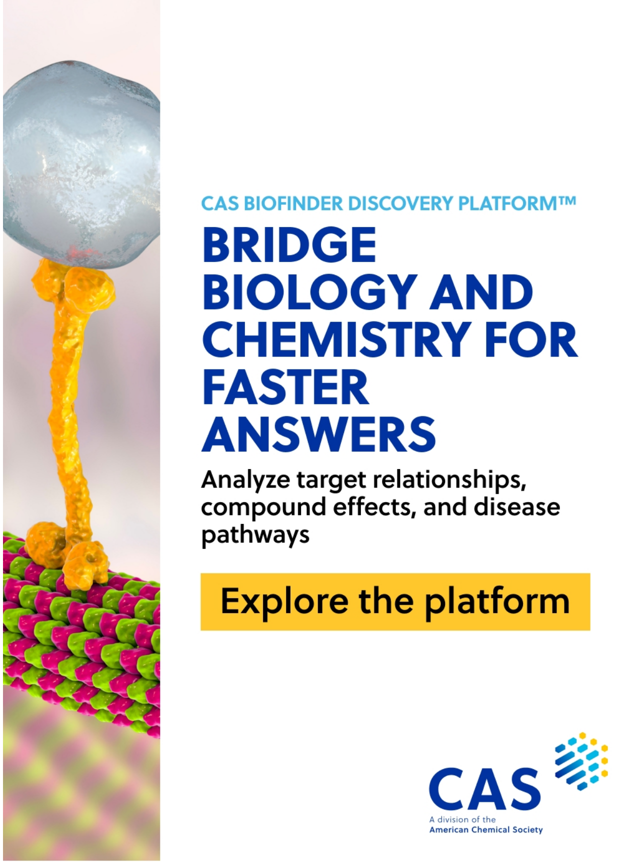

CAS BIOFINDER DISCOVERY PLATFORM™

BRIDGE BIOLOGY AND CHEMISTRY FOR FASTER ANSWERS

Analyze target relationships, compound effects, and disease pathways

Explore the platform

CAS
A division of the American Chemical Society